Multiproxy Reduced-Dimension Reconstruction of Pliocene Equatorial Pacific Sea Surface Temperatures

J.B. Wycech[1,2], E. Gill[1,3], B. Rajagopalan[4,1], T.M. Marchitto Jr.[2,5] and P.H. Molnar[1,2]

[1]Cooperative Institute for Research in Environmental Sciences, Boulder, Colorado, USA

[2]Department of Geological Sciences, University of Colorado Boulder, Boulder, Colorado, USA

[3]Now at Zillow Group, Seattle, Washington, USA

[4]Department of Civil, Environmental and Architectural Engineering, University of Colorado Boulder, Boulder, Colorado, USA

[5]Institute of Arctic and Alpine Research, University of Colorado Boulder, Boulder, Colorado, USA

Corresponding author: Jody Wycech (jody.wycech@colorado.edu)

Key Points:

- Pliocene equatorial Pacific sea surface temperatures were warmer than modern everywhere, with largest anomalies in the east
- A mean El Niño-like state, characterized by a reduced zonal sea surface temperature difference, prevailed in the Pliocene equatorial Pacific
- Pliocene Indian Summer Monsoon is estimated to have been ~20-40% weaker than modern

Abstract

A controversial aspect of the Pliocene climate system is a posited permanent sea-surface temperature (SST) distribution resembling that during El Niño events, which is largely inferred from sea-surface temperatures reconstructed from several sites in the equatorial Pacific. We utilize a reduced-dimension methodology on a compilation of previously published multiproxy (Mg/Ca, $U^{k'}_{37}$, TEX_{86}, and foraminifer assemblages) Pliocene SST records from the equatorial Pacific to reconstruct spatial and temporal snapshots of SST anomalies and a time series of Niño indices from 5 to 1 Ma. The use of multiple proxies increases the number of study sites and thereby improves the robustness of the reconstruction. We find that the early Pliocene equatorial Pacific was characterized by a reduced zonal SST difference due to minimal change in the west and extreme warmth in the east which peaked at 4.3 Ma. The intensity of this mean El Niño-like SST state then gradually diminished toward modern conditions. We also use the Pliocene Niño 4 time series to estimate the past strength of Indian Summer Monsoon given the modern correlation of it to the Niño 4 index. Results indicate the monsoon was weaker throughout the study interval with weakest conditions (~37% less rainfall than modern) occurring at 4.3 Ma, congruent with regional proxy records. In summation, this reduced-dimension approach spatially and temporally resolves the warm mean state of the Pliocene equatorial Pacific and has numerous applications to inferences of paleoclimate conditions in distal regions teleconnected to El Niño today.

Plain Language Summary

The Pliocene Epoch (5.3-2.6 million years ago) is the most recent time interval in Earth history when atmospheric carbon dioxide concentrations may have been similar to today and the continents were in their current configuration. For these reasons, Pliocene paleoclimate reconstructions are considered to be a useful indicator of conditions expected by the end of the 21st century. Several marine-derived Pliocene reconstructions from the equatorial Pacific suggest a sea-surface temperature (SST) distribution that resembles SSTs during El Niño events today. El Niño events have widespread impacts including reduced marine productivity in the eastern equatorial Pacific and weakened Indian Summer Monsoon. Insights into Pliocene El Niño-like SSTs are typically based on paleoclimate reconstructions from a few sites that are then used to infer regional conditions. In this study, we apply a statistical method to a compilation of nine Pliocene SST records across the equatorial Pacific to fill in the spatial gaps in the paleotemperature reconstructions. Our maps of reconstructed Pliocene SSTs reveal that the eastern equatorial Pacific was 3-6°C warmer than today, which is consistent with a mean El Niño-like state. Given the modern El Niño-Indian Summer Monsoon relationship, we estimate that Pliocene monsoon was ~20-40% weaker than today.

1 Introduction

The Pliocene (ca. 5.3-2.6 million years ago) is the most recent time interval in Earth history when global climate was warmer than the present (e.g. Fedorov et al., 2013; Salzmann et al., 2011) and when atmospheric CO_2 concentrations may have been comparable to those of the modern 400-ppm world (Martínez-Botí et al., 2015; Pagani et al., 2010; Seki et al., 2010). For these reasons, the Pliocene is considered a potential analog for climate conditions predicted for the latter part of this century (Crowley, 1996; Dowsett et al., 1996; Dowsett & Robinson, 2009). Not surprisingly, Pliocene climate model simulations with concentrations of CO_2 greater than those of pre-industrial time (Burls et al., 2017; Chandan & Peltier, 2018; 2017; Haywood et al., 2010; 2013; Lunt et al., 2008; Salzmann et al., 2013) and/or with assumed or simulated reduced northern hemisphere ice cover (e.g., Feng et al., 2017; Haywood & Valdes, 2004; Howell et al., 2016) lead to higher temperatures at mid and high latitudes. Other model runs, however, that exploit perturbations to equatorial Pacific SSTs can also lead to warmer mid and high-latitudes (e.g., Barreiro et al., 2005; Brierley & Fedorov, 2010; Burls & Fedorov, 2014a, 2014b; Goldner et al., 2011; Shukla et al., 2009, 2011; Vizcaíno et al., 2010). Thus, mimicking global warmth alone does not provide a good test of what processes made the Pliocene warmer than pre-industrial time (e.g., Fedorov et al., 2006), and investigations of regional differences in climate are needed.

Previous Pliocene reconstructions indicate that El Niño-like conditions prevailed across the equatorial Pacific, as evidenced by anomalously warm SSTs and a deep thermocline in the east (Cannariato & Ravelo, 1997; Chaisson & Ravelo, 2000; Dekens et al., 2008; Fedorov et al., 2013; Ford et al., 2012, 2015; Lawrence et al., 2006; Molnar & Cane, 2002; Philander & Fedorov, 2003; Ravelo et al., 2006; Seki et al., 2012; Wara et al., 2005), high sea-surface salinities in the west (Wycech, 2017), and a relatively shallow thermocline in the west (Chaisson & Ravelo, 2000). Furthermore, global Pliocene temperature and precipitation patterns resemble those produced during the strongest El Niño event in the historical record (1997-1998; Molnar & Cane, 2007). Modern El Niño events occur every 2-7 years when the atmospheric Walker Circulation relaxes (Bjerknes, 1969; Julian & Chervin, 1978). Such interannual El Niño events, however, cannot be explicitly resolved on geologic timescales because samples from the deep-sea climate archive are temporally blended by slow sedimentation and bioturbation (Anderson, 2001; Goreau, 1977; Schiffelbein, 1984). Thus, Pliocene SST reconstructions in the equatorial Pacific reflect mean conditions rather than the quasi-periodic El Niño events that occur today.

Inferences of the mean state of Pliocene El Niño are typically derived from reconstructions at strategically located sites across the equatorial Pacific. Inferring regional ocean conditions from one spatial data point is risky, however. Proxies used for the reconstruction are susceptible to local perturbations in hydrography or sedimentary preservation. For example, down-core variations in the preservation of the shells of foraminifera, carriers of the Mg/Ca paleotemperature proxy, can produce temporal shifts in reconstructed SST records that are unrelated to ocean warming or cooling (Wycech et al., 2018). Furthermore, local changes in upwelling or turbidity may alter the depth habitat of the organisms that carry the proxies assumed to record sea surface conditions (Schiebel et al., 1997; Schmuker, 2000; Schmuker & Schiebel, 2002; Wycech, 2017). On longer time scales such as that of the Pliocene, some sites may also record the influences of local tectonic events, such as the emergence of the Galapagos Islands on both sides of the equator (Karnauskas et al., 2017), which may lead to erroneous inferences in regional SST change through time.

To alleviate these issues, several previous studies have applied alternative statistical approaches to reconstruct time series (e.g. Kaufman et al., 2009; Lee et al., 2008; Li et al., 2010; Mann et al., 2008; Moberg et al., 2005) or full field maps (e.g. Cook et al., 1999; Gill et al., 2016a, 2016b; Kaplan et al., 1998; Luterbacher et al., 2004; Mann et al., 1998, 2008; Tierney et al., 2019; Tingley & Huybers, 2010) of climate conditions in the geologic past. Similarly, in this study we compiled previously published multi-proxy SST records spanning 5-0 Ma across the equatorial Pacific and used principal component analysis (PCA) to reconstruct well-resolved maps of Pliocene SST anomalies. Relative to typical methods used to infer conditions from a few records, our statistical approach provides a more rigorous assessment of the mean strength of the Walker Circulation during the Pliocene. Furthermore, it allows us to calculate Niño indices and thereby estimate the strength of Indian Summer Monsoon.

2 Data

Our application of PCA uses the relationship between the contemporary SSTs in the full field (gridded map, Figure 1b) and limited field (discrete spatial points, Figure 1c) to reconstruct the paleo-SST full field from only the limited field paleo-SST dataset.

2.1 Contemporary Data

Monthly SSTs from the equatorial Pacific region from 16°S to 16°N and 100°E to 60°W, gridded 2° × 2°from 1854 to 2018 are sourced from the NOAA National Climatic Data Center (NCDC) Extended Reconstruction Sea Surface Temperature (ERSST) version 3b data set (Smith et al., 2008). Monthly SST anomalies were calculated using the 1981-2010 climatology and averaged from May to the following April to produce annual averages. The averaging over May to April enables us to capture the annual El Niño Southern Oscillation (ENSO) signal as it is strongest during boreal winter.

2.2 Paleo SST Data

We compiled Pliocene SST records from four proxies: Mg/Ca, $U^{k'}_{37}$, TEX_{86}, and foraminifer assemblages (Table S1). Culturing experiments performed on living planktic foraminifera have shown that the magnesium content of their shells increases exponentially with increasing temperatures (e.g. Lea et al., 1999; Nürnberg et al., 1996). Alkenones are organic molecules produced by some species of marine phytoplankton (coccolithophores), and record temperatures by their degree of unsaturation (number of double bonds connecting carbon atoms). Specifically, the Unsaturation Index is defined by the ratio between the diunsaturated ($C_{37:2}$) alkenones to the sum of di- and triunsaturated ($C_{37:3}$) alkenones, $U^{K'}_{37} = C_{37:2}/(C_{37:2} + C_{37:3})$ (Brassell et al., 1986; Marlowe et al., 1984; Prahl & Wakeham, 1987; Volkman et al., 1980). The TEX_{86} proxy is based upon the temperature correlation with the relative abundances of 86-carbon glycerol dialkyl glycerol tetraethers synthesized by archaea from the *Thaumarchaeota* phylum (Kim et al., 2008; Schouten et al., 2002). An ecological approach to paleotemperature reconstruction is transfer function analysis using planktic foraminifer assemblages (Imbrie & Kipp, 1971). This method uses abstract factor analysis on foraminifer census data from core-top samples to determine the relative contribution, or factor, of each species to the assemblage. These factors are then input into multiple regression to calibrate a transfer function that is applied to down-core assemblage data and used to reconstruct past SSTs.

Although SST records have been published for 16 sites in the Pliocene equatorial Pacific, we use only the records (from 9 sites in total) that have temporal coverage from the Pliocene to the Late Pleistocene (<0.5 Ma; Figure 1c-d, Table 1). Some sites lie outside of the regions commonly used to quantify El Niño states, but are still affected by El Niño (e.g. ODP Site 1143). We include these sites in the reconstruction to increase the amount of variability captured by the limited field PCA and thereby improve the fidelity of the full field reconstruction. We required that the three youngest samples be less than or equal to 0.5 Ma in age to calculate the mean SST from 0-0.5 Ma, which we use to define the Pliocene SST anomalies. In cases where multiple SST records were present within the same 2° × 2° grid point, we used the record that had the longest duration if it had a comparable or higher temporal resolution than other sites in the same grid cell. The temporal resolution of the selected records range from 2-201 ka. Inter-site differences in sampling resolution are not problematic as the raw SST records (Figure 1d) are smoothed (Figure 1e) prior to PCA. The Mg/Ca and TEX_{86} records are located in both the west and east Pacific. By contrast, the one $U^{k'}_{37}$ record is located only in the east, and the assemblage-based records are only in the central and west Pacific.

The previously-published SSTs were calculated with a variety of calibrations. For consistency, we recalculated SSTs from Mg/Ca ratios, $U^{k'}_{37}$, and TEX_{86} using one calibration for each proxy. The raw TEX_{86} values were converted to temperature using the calibration of Kim et al. (2010), which does not include the (sub)polar sites. The raw $U^{k'}_{37}$ values were converted to temperature using the global SST calibration of Müller et al. (1998). A new $U^{k'}_{37}$ temperature calibration using a Bayesian spline regression model (BAYSPLINE; Tierney & Tingley, 2018) has been proposed to address the temperature limit of $U^{k'}_{37}$ at the warm extreme ($U^{k'}_{37} > 0.8$). Although the temperatures reconstructed using BAYSPLINE do not have a maximum limit, the uncertainties at the warm end are large (up to 4.4°C at 29.4°C). Although $U^{k'}_{37}$ values at ODP Site 846 in the East Pacific are high (approaching 1), the full field SST reconstruction using BAYSPLINE with a prior standard deviation of 10°C is no more than 0.5°C higher than that derived from the Müller et al. (1998) calibration. Thus, the $U^{k'}_{37}$-derived SSTs calculated using these two calibrations are not distinguishable from one another within errors reported in each (Figure A1a).

The Mg/Ca-based SSTs were calculated using the *T. sacculifer* calibration of Dekens et al. (2002). This Mg/Ca-temperature calibration includes a dissolution correction based on water depth that is deemed appropriate for SST reconstruction since foraminifer dissolution is prevalent in the equatorial Pacific (e.g. Fehrenbacher and Martin, 2011; Mekik et al., 2007; Rongstad et al., 2017; Rosenthal et al., 2000; Thompson and Saito, 1974; Wycech et al., 2018). Although the degree of dissolution likely varied slightly through the study interval (Pälike et al., 2012), a temporal adjustment to ΔCO_3^{2-} has a negligible effect on the reconstructed SST trend (see Appendix). More critically, our SST calculations include a correction for lower Mg/Ca ratios of Pliocene seawater (Mg/Ca_{sw}) provided by Zeebe and Tyrrell (2019). The correction for lower Mg/Ca_{sw} entailed multiplying the Mg/Ca-temperature pre-exponential constant by the ratio of paleo to modern Mg/Ca_{sw} (*sensu* Medina-Elizalde et al., 2008) where modern Mg/Ca_{sw} is 5.17 mol/mol (Rausch et al., 2012). Relative to the SSTs calculated with only the water depth correction, the Mg/Ca_{sw} adjustment increases SSTs by 1.5°C on average with the adjustments being smallest for the youngest samples (~0.1°C) and largest at ~5 Ma (2.5-2.6°C; Figure A1b-d).

Each reconstructed SST datum reflects average conditions over several thousand years given the mean sampling interval at the study sites (1.81 cm) and the relatively slow Plio-Pleistocene sedimentation rates in the west (2.7-4.7 cm/kyr at Site 806) and east (2.1-3.8 cm/kyr at Site 850) Pacific. We smoothed the raw SST records using a local polynomial method, i.e. a second order polynomial with 20% of the nearest data points (e.g., Loader, 1996) in order to obtain an SST value at any selected interval between 2-5 Ma (Figure 1e). The use of a larger local neighborhood (~70%) produced the same results as the smaller (20%), but the use of a smaller neighborhood is more appropriate for the long study period (5 million years) and sampling resolution. Specifically, 20% nearest neighbors equates to temporal smoothing windows of ~1 Ma for the $U^{k'}_{37}$, Mg/Ca, and foraminifer assemblage records and ~2 Ma for the TEX_{86} records.

We converted these SST records to anomalies by subtracting the 0-0.5 Ma average from each respective smoothed time series. The 0-0.5 Ma interval was selected as the base for anomaly calculations in order for the study to include more sites that would have otherwise been eliminated due to their pre-Holocene core tops (e.g. sites 1241 and 806). Furthermore, the interval from 0-0.5 Ma includes multiple data points (3-288) from each record, which reduces the likelihood of aliasing. The inclusion of multiple glacial-interglacial cycles in the past 0.5 Ma introduces a cold bias into the base period 0-0.5 Ma. Because of this bias, we describe SST anomalies in reference to the “base period” (0-0.5 Ma), and not the modern, instrumental period or the Holocene.

3 Reconstruction Method

We use the same PCA technique described in Gill et al. (2016b), and we briefly review the technique in the specific context of this study (Figure S1).

3.1 Principal Component Analysis (PCA)

PCA entails decomposition of multi-variate space-time data into orthogonal space-time components, also referred to as modes, by eigen decomposition of the covariance matrix (see Von Storch and Zwiers, 2001). The spatial components are in the eigenvectors, also known as Empirical Orthogonal Functions (EOFs) while the temporal modes are the Principal Components (PCs). Projecting the PCs onto the eigenvectors transforms to the original data space. The components are ordered according to the percentage of total variance resolved such that the first few components capture most of the variance.

Application of PCA to paleoclimate SST reconstruction relies upon the spatial and temporal variability of the modern SSTs observed at each site. For this reason, we first performed a PCA on the full field of contemporary SSTs within the defined equatorial Pacific domain (16°N-16°S, 100°E-60°W) using the complete historical SST record (1854-2018) to maximize the amount of data input into the contemporary PCA. The first three modes were retained as they together explain 81% of the total variance in the historical record (Figure A2). Next, we performed a PCA on the contemporary SSTs in the limited field, i.e. the spatial grid points with paleo-SST records. From this, the first two modes were retained as they together explain 83% of the total variance. Each of three PCs from the full field PCA are linearly regressed against the two PCs of the limited field – thereby fitting three linear regression models. For each selected time point, say 2 Ma, the paleo-SST anomaly at each site is multiplied by the contemporary limited field eigenvector matrix to obtain the limited field paleo PCs. Estimates of the three PCs of the full field are obtained using the linear regression models. The three PCs of the full field are projected back to the SST-anomaly space by multiplication with the full field eigenvectors to reconstruct the full field of paleo-SST anomalies. We repeated this procedure at discrete time points (2, 3, 4, 4.3 Ma, and 5 Ma) to generate maps of equatorial Pacific SST anomalies. Reconstructions were also performed at small time-steps (0.02 Ma) from 5-1 Ma to generate a time series of the Niño indices (Niño 4 = 5°N to 5°S and 160°E to 150°W, Niño 3.4 = 5°N to 5°S and 170°W to 120°W, Niño 3 = 5°N to 5°S and 150°W to 90°W, Niño 1+2 = 0° to 10°S and 90°W to 80°W) and the Western Trans-Niño Index (WTNI). WTNI is calculated by subtraction of WPAC (5°N to 5°S and 120°E to 160°E) from Niño 1+2 (Trenberth & Stepaniak, 2001). Niño indices are defined as the mean SST anomalies in each respective region, and provide a quantitative means to monitor the state of ENSO in the equatorial Pacific. For example, development of modern El Niño events is apparent by increases in Niño 1+2 and WTNI due to positive SST anomalies in the eastern equatorial Pacific. PCA provides the means to calculate Niño indices for quantitative assessment of paleo-El Niño, which is otherwise not possible using the conventional comparison of temperature records from only a 2-3 sites across the equator.

The uncertainty in the reconstruction was quantified by generating 500 ensembles of the full field PC estimates using the standard errors in the PCs from the regression models. Consequently, the ensembles of SST anomalies provide nominal estimates of uncertainty from the regression estimates of the PCs. While useful, this approach tends to underestimate the full standard error because it does not include the uncertainties in the regression model parameters and data. Future studies should consider Bayesian regression methods, which provide robust estimates of uncertainty by incorporating all sources of error (see Gelman & Hill, 2007).

3.2 Calibration of PCA Model

We performed calibration and validation tests to assess the estimates of past SSTs by reconstructing contemporary SSTs using the same limited field PCA approach (see Section A2). We first compared actual and reconstructed historical time series of Niño indices (Figure 2a). Reconstructed SSTs agree best with the observed Niño indices for strong La Niña and El Niño events. Model-data mismatch is greatest for Niño 4 and Niño 3.4 due to the sparsity of limited-field locations in these regions. Conversely, reconstructed SSTs best match the observed Niño 1+2 time series due to the numerous sites in the eastern equatorial Pacific. Although model-data mismatches exist where anomalies are not large, reconstructed SSTs capture the observed Niño indices for the two strongest El Niño events (1982-1983, 1997-1998) and the three strongest La Niña events (1973-1974, 1988-1989, 2010-2011) in the historical record (Figure 2a).

We then compared actual and reconstructed maps of SST anomalies for the aforementioned two strongest El Niño events (Figure 2b). For the 1982-1983 El Niño, reconstructed SSTs capture a maximum SST anomaly of 1.8°C, which has the same spatial pattern of warming and is within 0.4°C of the observed conditions (Figure 2b left). Similarly, the reconstructed 1997-1998 SST anomalies show warming in both the eastern and central equatorial Pacific up to 3°C, within 0.7°C of those observed (Figure 2b right). In summation, the numerous study sites in the region most affected by El Niño (from the eastern equatorial Pacific) enable accurate reconstruction of SSTs and bolster confidence in our reconstruction of paleo-El Niño-like SST distributions.

3.3 Assumptions

Applying the limited field approach to paleoclimate reconstructions requires several assumptions. First, we assume that the relationships among sites in the limited field are linearly related to relationships within the full field for the contemporary period. Second, we assume spatiotemporal variation in the contemporary SST record apply as far back at 5 Ma. This is an acceptable assumption given the warm eastern Pacific Pliocene SSTs and that modern ENSO teleconnections are evident among global Pliocene climate records (Fedorov et al., 2006; Lawrence et al., 2006; Molnar & Cane, 2002, 2007; Philander & Fedorov, 2003; Ravelo et al., 2006; Wara et al., 2005). Third, we consider the temperature-proxy relationships observed in laboratory culture or in modern sediments to be applicable back to 5 Ma. Relatedly, we assume that ontogenies of the biological carriers of the Mg/Ca, TEX_{86}, and $U^{k'}_{37}$ proxies did not change between the Pliocene and today. Fourth, we consider the proxies to record annual average SSTs throughout the equatorial Pacific. Although seasonality is low in the tropics, the assumption carries risk because the biological carriers of the proxies can sometimes prefer specific seasons or greater water depths (Harada et al., 2001; Leduc et al., 2010; Müller & Fischer, 2001; Ohkouchi et al., 1999; Rae et al., 2014). Finally, we acknowledge that the SST reconstruction reflects the mean state of the equatorial Pacific due to the time-averaging within single deep-sea samples, and therefore, our results do not elucidate interannual ENSO variability. A mean El Niño-like state may indicate increased ENSO amplitude and/or frequency, or simply an increase in SST without a change in interannual variability.

4 Results – Pliocene Reconstructions

4.1 Limited Field SST Reconstruction

Prior to reconstructing the paleo full field of SST anomalies, we assess how well the method reconstructs each paleo-SST record (Figure 3). The goodness of fit between the reconstructions from our method and the smoothed paleo-SSTs were determined using the root mean square error (RMSE), noted in the upper right corner of each scatterplot. The reconstructions were performed at 0.5 Ma intervals from 5-0 Ma (sample size=11). The first two eigenvector values are provided for each site and correspond to the circles mapped in Figure A3. These EOF values indicate the relative contribution of these data to the reconstruction of the full field. The RMSE values are typically within the error of the temperature reconstruction (1.2-2.2°C, ±SE), reaching 1.5°C for the poorest fits. The use of multiple proxies may explain some of the larger RMSE values. For example, foraminifer assemblages indicate less to no warming relative to nearby Mg/Ca-based records.

4.2 Equatorial Pacific SST Reconstruction

Figure 4a-e shows reconstructed SST anomaly maps for 5, 4, 4.3, 3, and 2 Ma. The reconstruction at 4.3 Ma is provided to illustrate the spatial distribution of SST anomalies during peak warming. These spatial snapshots are accompanied by a time-series of the Niño indices, WTNI, and the absolute zonal SST difference generated by PCA analysis at 20 ka time steps (Figure 5a).

Warm SSTs prevail across the equatorial Pacific from 5-2 Ma with more extreme warming in the eastern and central than western equatorial Pacific. SST anomalies, up to 4.5°C near the coast of South America, are present at 5 Ma with SST anomalies of 2°C reaching as far as 165°E (Niño 4 =1.6°C, Figure 4e and 5b). The warming in the central and eastern Pacific increases to a maximum at 4.3 Ma (Niño 1+2 = 4.3°C, Niño 3.4 = 3.5°C; Figure 5a) with an inferred warming of 4.8°C off the coast of Peru (Figure 4d). Meanwhile, SSTs in the western equatorial Pacific were within 1.5°C of base period conditions through the study interval reaching a maximum at 5.0 Ma (WPAC = 0.7°C) and a minimum at 4.0 Ma (WPAC = -1.1°C). After 4.3 Ma, long-term cooling occurred across the equatorial Pacific with maximum anomalies in the easternmost Pacific of 4.3°C, 2.8°C, and 1.6°C at 4 Ma, 3 Ma, and 2 Ma, respectively (Figure 4a-c). The standard errors on the SST anomalies are relatively small for all temporal snapshots, 0.1-0.3°C for most of the equatorial Pacific with maximum errors of 0.4°C immediately off the coast of South America where anomalies are greatest (Figure 4f-j).

The time series of Niño indices (Figure 5a) illustrate this temporal pattern of peak equatorial warming at 4.3 Ma (Niño 4 = 2.0°C, Niño 1+2 = 4.3°C) with subsequent gradual cooling toward base-period conditions. The zonal SST difference across the Pliocene equatorial Pacific is of interest because warming in the east occurs when the Walker Circulation weakens and El Niño events occur today. Although warming in the Pliocene east Pacific alone is consistent with an El Niño-like SST pattern, Zhang et al. (2014) argue that the Pliocene equatorial Pacific had a modern west-east SST difference due to uniform warming everywhere. We reconstruct time series of the WTNI using anomalies and absolute temperatures ($\Delta SST_{West\text{-}East}$) to quantify the zonal SST difference from 5-1 Ma (Figure 5a). The positive WTNI in early Pliocene time indicates greater warmth in the east than west and a reduced zonal SST difference relative to the base period. We also calculate $\Delta SST_{West\text{-}East}$ by subtracting the WTNI from the 0-0.5 Ma average SST difference between the Niño 1+2 and WPAC regions (8.4°C).

Our Pliocene results are consistent with an El Niño-like SST pattern given that the WTNI values are positive (Figure 5a), the Pliocene $\Delta SST_{West\text{-}East}$ values are lower than the 0-0.5 Ma average (Figure 5a), and the eastern equatorial cold tongue is diminished. The largest WTNI (4.4°C) and lowest $\Delta SST_{West\text{-}East}$ (4.0°C) occur at 4.14 Ma, the former of which is 1.2°C larger than the WTNI observed during the 1997-1998 El Niño, and the inferred SST pattern resembles a strong El Niño (Figure 5b). The $\Delta SST_{West\text{-}East}$ minimum occurs ~200,000 years after peak warmth in the east due to cooling in the WPAC region from 4.3-4 Ma (Figures 4c-d and 5a). The eastern equatorial Pacific gradually cools after 4 Ma, but the zonal SST difference does not reach base-period conditions until ~1.5 Ma (Figure 5a).

5 Discussion

5.1 Proxy sensitivity to PCA Reconstruction

We investigated the sensitivity of the PCA reconstruction on the type of proxy included in the limited field dataset (see supporting information). The first three iterations used a multi-proxy approach in which either the $U^{k'}_{37}$, Mg/Ca, or TEX_{86} records were respectively removed and, whenever possible, replaced by a different proxy type from the same site. Results from these iterations indicate that removal of the $U^{k'}_{37}$ or TEX_{86} proxies changed the full field reconstruction by less than ~0.5°C (Figures S2 and S4) while removal of the Mg/Ca proxy changed the full field reconstruction by less than ~1.5°C (Figure S3).

An additional three iterations used a single proxy approach based on only $U^{k'}_{37}$, Mg/Ca, or TEX_{86}. The largest difference (2.1-3.3°C) between these iterations (Figures S5-S7) and the original (Figure 4) occurred when the reconstruction was based only on TEX_{86} records (Figure S7). We further compared the minimum zonal SST difference (-WTNI; Table S2) and the west-east SST difference ($\Delta SST_{West\text{-}East}$) reconstructed by each iteration (Figure S8). The Mg/Ca-only and TEX_{86}-only iterations have the largest divergence from the original reconstruction because these iterations are based on only 4 SST records compared to the 9 records used for the complete, multi-proxy reconstruction (Table S2). By contrast, the minimum zonal SST differences from iterations 1-4 (-3.4°C to -4.3°C) are similar to that of the original reconstruction (-4.4°C) and reproduce the trend and magnitude of the original $\Delta SST_{West\text{-}East}$ time series (Table S2, Figure S8). Agreement between the original reconstruction and the majority of the iterations indicates that 1) the inferred reduced zonal SST gradient is robust and 2) the reconstruction benefits from numerous SST records even when they are derived from multiple proxies. Some previous Pliocene reconstructions indicate the zonal SST difference across the equatorial Pacific was modern-like (e.g., Zhang et al., 2014; Tierney et al., 2019), which differs from the reconstruction presented herein. A potential explanation for such conflicting results is that the prior studies often use only one or two proxies and/or are focused on the mid-Pliocene warm period (3-3.3 Ma) when mean El Niño-like conditions were likely subsiding.

5.2 Pliocene El Niño-like SST distribution

Prior to this study, evidence for the Pliocene mean SST state resembling that during peak El Niño events was based on SST and thermocline reconstructions from a few strategically located sites across the equatorial Pacific (e.g. Ford et al., 2012; Lawrence et al., 2006; Ravelo et al., 2006; Seki et al., 2012; Wara et al., 2005). We provide a broader reconstruction of SST anomalies across the region as well as quantifying Niño indices and the zonal SST difference. The results presented herein support mean early Pliocene El Niño-like SSTs, characterized by a warm central and eastern equatorial Pacific and a reduced zonal SST difference (Figures 4a-e and 5a; Dekens et al., 2008; Groeneveld et al., 2006; Lawrence et al., 2006; Ravelo et al., 2006, 2014; Seki et al., 2012; Steph et al., 2006; Wara et al., 2005). The magnitude and spatial pattern of warming across the equatorial Pacific during the early Pliocene was more extreme than the strongest El Niño event in the historical record (1997-1998; Figure 2b). This finding supports the inference that the 1997-1998 El Niño is the best modern analog for Pliocene conditions (Molnar and Cane, 2007).

Previous studies suggest El Niño conditions terminated ~4 Ma due to the hypothesized closure of the Central American and/or Indonesian Seaways (Cannariato & Ravelo, 1997; Chaisson & Ravelo, 2000; Steph et al., 2010; Zhang et al., 2012). By contrast, our reconstructions indicate slow, long-term deterioration of El Niño-like conditions after 4.1 Ma (see WTNI and $\Delta SST_{West\text{-}East}$ time series in Figure 5a) such that a perturbation to the ocean-climate system by a single tectonic event cannot explain the shift toward modern conditions.

Modern El Niño events impact global precipitation and temperature patterns (Ropelewski & Halpert, 1996). Some general circulation models with a warm eastern equatorial Pacific do not yield major large-scale anomalies like those during El Niño (Bonham et al., 2009; Haywood et al., 2007), but others are able to simulate such teleconnections (e.g., Barreiro et al., 2005). Although high SST anomalies in the east are a salient feature of the Pliocene equatorial Pacific, our study does not elucidate how this El Niño-like SST pattern affects global temperatures.

5.3 Constraints on Pliocene Indian Summer Monsoon Rainfall

Since the Pliocene is considered to be an analog for future climate conditions, reconstructing Pliocene Indian summer monsoon bears on relative rainfall changes expected in the region by the end of the 21st century. Warming in the central equatorial Pacific during modern El Niño events weakens Indian Summer Monsoon rainfall via atmospheric teleconnection (e.g., Krishna-Kumar et al., 2006). We pair this modern observation with our Pliocene equatorial Pacific SST reconstruction to estimate the strength of Pliocene monsoon. Rainfall anomalies (Pliocene-base period) are calculated using the paleo-Niño 4 time series (Figure 5a) and the modern correlation between Niño 4 and scaled monsoon precipitation (Indian Institute of Tropical Meteorology; $ISM_{precip,scaled} = -1.91 \times \text{Niño4} + 0.11$, $R^2 = 0.25$). The Niño 4 region is warmer than the base period from 5-1 Ma, which produces negative rainfall anomalies, i.e. drier conditions throughout the study interval (Figure 6a). Our most extreme estimate suggests the monsoon could have been ~37% weaker than today during the interval with the most intense equatorial Pacific warming (4.3 Ma).

Evidence for weaker Indian Summer Monsoon during the Pliocene relative to today is spatially pervasive in both marine and continental realms (Figure 6b) and consistent with Pliocene climate model results (e.g. Brierley & Fedorov, 2010; Fedorov et al., 2013). Relative to modern, early Pliocene sediments from the Bay of Bengal have lower accumulation rates, reduced concentrations of run-off proxies (Mn, Fe, K/Al), higher calcium carbonate content, smaller particle sizes, more weathered clays, and lower abundances of a benthic foraminifer that prefers high productivity waters (Burbank et al., 1993; Clift et al., 2008; Gourlan et al., 2008; Gupta & Thomas, 2003; Prell & Kutzbach, 1997). Similarly, the Indus Fan and Yuanmou Basin have lower sedimentation rates (Chang et al., 2010; Clift et al., 2008) and the $\delta^{18}O$ values of calcite cements within the Siwalik Sandstone at Surai Khola suggest more arid conditions from 4-2 Ma (Sanyal et al., 2005). The pervasive evidence for higher residence times of sediments within the floodplain, drier conditions, and less Pliocene continental weathering relative to present-day is consistent with weaker monsoon rainfall, particularly around 4.3 Ma.

6 Conclusion

We use a multi-proxy reduced-dimension methodology on previously published equatorial Pacific SST records spanning 5-0 Ma to reconstruct spatial and temporal images of the Pliocene mean El Niño-like state. We find that the Pliocene equatorial zonal SST difference across the Pacific was reduced by ~4.4°C relative to the comparison period (0-0.5 Ma) due to extreme warming of up to 4.8°C in the east and minimal warming in the west. The warming peaked at 4.3 Ma, and gradually declined towards the modern (La Niña-like) state. The added value of our approach is the production of high spatial resolution maps (2° × 2°) of SST anomalies, which allows for the calculation of Niño indices and estimates of precipitation/temperature anomalies in distal regions teleconnected to El Niño. We provide an estimate of the strength of Pliocene Indian Summer Monsoon based on the paleo-Niño 4 reconstruction. Our results suggest the Pliocene monsoon may have been ~16-37% weaker than the 0-0.5 Ma average, which is consistent with continental and marine geological evidence from the region. In summary, our results support the argument for the Pliocene mean El Niño-like state and supply quantitative estimates on the strength of paleo-ISM. We further conclude that our reconstruction of a reduced zonal SST gradient is more robust than previous studies due to the multi-proxy approach that improves spatial coverage of paleo-SST data across the equatorial Pacific.

Acknowledgments

Funding courtesy the CIRES Visiting Postdoctoral Fellowship (Wycech). Contemporary data used in this study is available within the IRI Climate Data Library (iridl.ldeo.columbia.edu). All data analysis was done in R (R Core Team, 2014). We also thank the associate editor and two anonymous reviewers for their suggestions that helped improve the manuscript.

Appendix A: Detailed Research Methods

This appendix provides further details on the SST reconstruction from $U^{k'}_{37}$ and Mg/Ca measurements, PCA output, and the calibration and validation of the model.

A1. SST Reconstruction from $U^{k'}_{37}$ and Mg/Ca Ratios

We compared $U^{k'}_{37}$-based SSTs reconstructed using the linear calibration of Müller et al. (1998) (M98 hereafter) and BAYSPLINE (Tierney and Tingley, 2018; Figure A1a). At 4.3 Ma, SSTs reconstructed with both calibrations reach maxima of 28.4°C using M98 and 30.4°C using BAYSPLINE. The BAYSPLINE-derived SSTs, which applied a conservative prior standard deviation of 10°C, are on average 0.6°C less than those calculated with M98 after 2 Ma, but are on average 0.8°C higher than those calculated with M98 from 4-5 Ma. The difference between the linear- and BAYSPLINE-calculated SSTs, however, are within one standard error of either calibration (±1.5°C from M98; 1.4-4.4°C from BAYSPLINE).

Our SST reconstruction from foraminiferal Mg/Ca ratios entails two adjustments, one for dissolution and one for the history of ratios of Mg/Ca in seawater, Mg/Ca_{sw} (see Section 2.2, Figure A1b-d). We compare our Mg/Ca-based SST time series to those reconstructed with the two *T. sacculifer* calibrations from Dekens et al. (2002) that correct for dissolution either based on water depth or the modern ΔCO_3^{2-} value (grey and red lines, respectively, in Figure A1b-d). We calculated the $\Delta CO_3^{2-}{}_{modern}$ at sites 806, 847, and 1237 (-11.5, -25.6, and -20.9 μmol/kg, respectively) using bottom water conditions and the program CO2SYS v.2.1 (Lewis and Wallace, 1998) with the default dissociation constants (Mehrbach et al., 1973), as refit by Dickson & Millero (1987). We obtained bottom water temperature, pressure, dissolved phosphate, and dissolved silica concentrations from the World Ocean Database 2013 (Boyer et al., 2013). Total alkalinity and total dissolved inorganic carbon values were obtained from GLODAP (National Center for Atmospheric Research Staff, 2014). The degree of dissolution may have varied through the study interval, and we investigated these effects by adjusting the ΔCO_3^{2-} values input into the Dekens et al. (2002) calibration using the published paleo-CCD time series (Pälike et al., 2012) and the modern equatorial Pacific ΔCO_3^{2-} depth relationship (ΔCO_3^{2-} decreases by 0.0136 μmol/kg per 1 m depth increase for water depths > 2000 m). This temporal adjustment to ΔCO_3^{2-} had a minimal effect on the reconstructed SST (<0.1°C). The SSTs calculated with the modern ΔCO_3^{2-} value are ~1.5° higher on average, with recent interglacials seemingly too warm, compared to those adjusted based on water depth, so we favor the latter.

There is robust evidence that Pliocene Mg/Ca_{sw} was lower than modern (Coggon et al., 2010; Fantle and DePaolo, 2006; Higgins and Schrag, 2012; Horita et al., 2002; Lowenstein et al., 2001; Zeebe and Tyrrell, 2019; Zimmermann, 2000), and a Mg/Ca_{sw} correction has been shown to reconstruct warmer-than-modern West Pacific SSTs (Medina-Elizalde et al., 2008; O'Brien et al., 2014) that are reasonable considering CO_2 forcing (Ford and Ravelo, 2018). At west Pacific Site 806, the average SST reconstructed with the Mg/Ca_{sw} correction are 0.5°C colder than the modern SST (29.3°C, 1981-2010 mean) from 3-0 Ma, but 0.5°C higher than modern from 5-3 Ma (Figure A1b). By contrast, the SSTs reconstructed with only the depth-based dissolution correction at Site 806 are 1.6°C colder than modern on average and do not have a temporal trend from 5-0 Ma.

A2. Principal Component Analysis (PCA) SST Reconstruction

Pliocene SST reconstruction via PCA entails use of the first few PCs of the limited field to model the first few PCs of the full field. The eigenvalues (λ) for each PC (Figure A2) were used to define the cut-off of PCs to include in the model. Although defining such a cut-off is arbitrary, it is important to include the appropriate number of PCs to maximize the amount of total variance captured while minimizing the amount of noise. We define the cut-off based on "knees" of the eigenvalue spectra, the smallest eigenvalues above the noise floor ($\lambda > 0.05$; represented by the plus signs in Figure A2).

We model the first three modes of the full field (λ_1= 0.594, λ_2= 0.141, and λ_3=0.074) using the first two modes of the limited field ($\lambda_1^\dagger$=0.737 and $\lambda_2^\dagger$=0.093). The limited field captures 83% of the total variance, but the spatial distribution of the eigenvector magnitude is not uniform across the region (Figure A3a-c). Specifically, EOF1 weightings are highest in the east equatorial Pacific. This information is useful for future drilling projects that aim to assess paleo-SST variability within the equatorial Pacific. We also assessed the effectiveness of the approach by comparing the actual (observed) and reconstructed eigenvalues for the first three PCs (Figure A3d-f). The model-data eigenvalue agreement bolsters confidence in the Pliocene SST reconstruction using this method.

A3. Model Calibration and Validation using β and R^2 Statistics

We use two criteria (*β* and R^2 statistics) to assess the ability of the model to reconstruct the contemporary full-field SSTs from the limited-field. The resolved variance statistic (*β*) is given by

$$\beta = 1 - \frac{\sum(y-\hat{y})^2}{\sum y^2} \qquad \text{(A1)}$$

where *y* is the contemporary data and $\hat{y}$ is the reconstructed data for the full period (1854-2017). The *β* statistic is computed at each grid point within the equatorial Pacific domain (Figure A4a). A *β* statistic equal to 1 indicates a perfect fit, and -1 indicates two random series. The *β* values range from 0.2 to greater than 0.9 across the reconstruction domain. The lowest *β* values occur in the western equatorial Pacific, where there are few/no limited-field sites. Conversely, the highest *β* values (up to 0.98) occur in the eastern equatorial Pacific with numerous limited-field sites.

The squared correlation statistic (R^2) indicates the strength of correlation between the observed and reconstructed SSTs at each grid point (Figure A4b). Similar to the calibration *β* map, the region with fewer limited-field sites, the western equatorial Pacific, has lower R^2 values (0.2-0.5) than the region with numerous limited-field sites, the eastern equatorial Pacific (R^2=0.70-0.98).

For model validation, we trained the PCA using only recent SSTs (1980-2013). We then reconstructed the full-field SSTs for the earlier contemporary period (1854-1979) using the trained PCA model, and computed the *β* and R^2 statistics to assess the fitting and correlation, respectively, between the observed and reconstructed SSTs (1854-1979). The validation *β* and R^2 values are lower than the calibration statistics in the western equatorial Pacific, again due to few limited-field sites (Figure A4c-d), but validation statistics for the eastern and central regions remain high (*β* = 0.50-0.97 and R^2 =0.5-0.99).

References

Anand, P., Elderfield, H., & Conte, M.H. (2003). Calibration of Mg/Ca thermometry in planktonic foraminifera from a sediment trap time series. *Paleoceanography 18*, 1–15.

Anderson, D.M. (2001). Attenuation of millennial-scale events by bioturbation in marine sediments. *Paleoceanography 16,* 352–357.

Barreiro, M., Philander, G., Pacanowski, R., & Fedorov, A. (2005). Simulations of warm tropical conditions with application to middle Pliocene atmospheres. *Climate Dynamics 26*, 349–365.

Bjerknes, J. (1969). Atmospheric teleconnections from the equatorial Pacific. *Monthly Weather Review 97,* 163–172.

Bonham, S.G., Haywood, A.M., Lunt, D.J., Collins, M., & Salzmann, U. (2009). El Niño–Southern Oscillation, Pliocene climate and equifinality. *Philosophical Transactions of the Royal Society A: Mathematical, Physical and Engineering Sciences 367*, 127–156. https://doi.org/10.1016/0031-0182(89)90130-2

Boyer, T.P., Antonov, J. I., Baranova, O. K., Coleman, C., Garcia, H. E., Grodsky, A., et al. (2013). World Ocean Database 2013 In Levitus, S., & Mishonov, A. (Eds.) *NOAA Atlas NESDIS* (vol. 72, pp. 1-209); Silver Spring, MD: U.S. Government Printing Office.

Brassell, S.C., Eglinton, G., Marlowe, I.T., Pflaumann, U., & Sarnthein, M. (1986). Molecular stratigraphy: a new tool for climatic assessment. *Nature 320,* 129–133. https://doi.org/10.1016/0016-7037(81)90012-0

Brierley, C.M., & Fedorov, A.V. (2010). Relative importance of meridional and zonal sea surface temperature gradients for the onset of the ice ages and Pliocene-Pleistocene climate evolution. *Paleoceanography 25,* 1-16.

Burbank, D.W., Derry, L.A., & France-Lanord, C. (1993). Reduced Himalayan sediment production 8 Myr ago despite an intensified monsoon. *Nature 364,* 48–50.

Burls, N.J., & Fedorov, A.V. (2014a). Simulating Pliocene warmth and a permanent El Niño-like state: The role of cloud albedo. *Paleoceanography 29,* 893–910. https://doi.org/10.1002/2014PA002644

Burls, N.J., & Fedorov, A.V. (2014b). What Controls the Mean East–West Sea Surface Temperature Gradient in the Equatorial Pacific: The Role of Cloud Albedo. *Journal of Climate 27,* 2757–2778. https://doi.org/10.1175/JCLI-D-13-00255.1

Burls, N.J., Fedorov, A.V., Sigman, D.M., Jaccard, S.L., Tiedemann, R., & Haug, G.H. (2017). Active Pacific meridional overturning circulation (PMOC) during the warm Pliocene. *Science Advances 3,* 1–13. https://doi.org/10.1126/sciadv.1700156

Cannariato, K.G., & Ravelo, A.C. (1997). Pliocene-Pleistocene evolution of eastern tropical surface water circulation and thermocline depth. *Paleoceanography 12,* 805–820.

Chaisson, W.P., & Ravelo, A.C. (2000). Pliocene development of the east-west hydrographic gradient in the equatorial Pacific. *Paleoceanography 15,* 497–505.

Chandan, D., & Peltier, W.R. (2017). Regional and global climate for the mid-Pliocene using the University of Toronto version of CCSM4 and PlioMIP2 boundary conditions. *Climate of the Past 13*, 919–942. https://doi.org/10.5194/cp-13-919-2017

Chandan, D., & Peltier, W.R. (2018). On the mechanisms of warming the mid-Pliocene and the inference of a hierarchy of climate sensitivities with relevance to the understanding of climate futures. *Climate of the Past 14*, 825–856. https://doi.org/10.5194/cp-14-825-2018

Chang, Z., Xiao, J., Lü, L., & Yao, H. (2010). Abrupt shifts in the Indian monsoon during the Pliocene marked by high-resolution terrestrial records from the Yuanmou Basin in southwest China. *Journal of Asian Earth Sciences 37*, 166–175. https://doi.org/10.1016/j.jseaes.2009.08.005

Clift, P.D. (2006). Controls on the erosion of Cenozoic Asia and the flux of clastic sediment to the ocean. *Earth and Planetary Science Letters 241*, 571–580. https://doi.org/10.1016/j.epsl.2005.11.028

Clift, P.D., Hodges, K.V., Heslop, D., Hannigan, R., Van Long, H., & Calves, G. (2008). Correlation of Himalayan exhumation rates and Asian monsoon intensity. *Nature Geoscience 1*, 875–880. https://doi.org/10.1016/S0012-8252(99)00054-9

Coggon, R.M., Teagle, D.A.H., Smith-Duque, C.E., Alt, J.C., & Cooper, M.J. (2010). Reconstructing Past Seawater Mg/Ca and Sr/Ca from Mid-Ocean Ridge Flank Calcium Carbonate Veins. *Science 327*, 1114–1117.

Cook, E.R., Meko, D.M., Stahle, D.W., & Cleaveland, M.K. (1999). Drought Reconstructions for the Continental United States. *American Meteorotological Society 12*, 1145–1162.

Crowley, T. (1996). Pliocene climates: the nature of the problem. *Marine Micropaleontology 27*, 3–12.

Dekens, P.S., Lea, D.W., Pak, D.K., & Spero, H.J. (2002). Core top calibration of Mg/Ca in tropical foraminifera: Refining paleotemperature estimation. *Geochemistry Geophysics Geosystems 3*, 1–29. https://doi.org/10.1029/2001GC000200

Dekens, P. S., Ravelo, A. C., & McCarthy, M. D. (2007). Warm upwelling regions in the Pliocene warm period. *Paleoceanography*, *22*(3), 1-12.

Dekens, P.S., Ravelo, A.C., McCarthy, M.D., & Edwards, C.A. (2008). A 5 million year comparison of Mg/Ca and alkenone paleothermometers. *Geochemistry Geophysics Geosystems 9*, 1–18.

Dickson, A.G., & Millero, F.J. (1987). A comparison of the equilibrium constants for the dissociation of carbonic acid in seawater media. *Deep Sea Research Part A. Oceanographic Research Papers 34*, 1733–1743.

Dowsett, H., Barron, J., & Poore, R. (1996). Middle Pliocene sea surface temperatures: a global reconstruction. *Marine Micropaleontology 27*, 13–25.

Dowsett, H.J., & Robinson, M.M. (2009). Mid-Pliocene equatorial Pacific sea surface temperature reconstruction: a multi-proxy perspective. *Philosophical Transactions of the Royal Society A: Mathematical, Physical and Engineering Sciences 367*, 109–125.

Fantle, M.S., & DePaolo, D.J. (2006). Sr isotopes and pore fluid chemistry in carbonate sediment of the Ontong Java Plateau: Calcite recrystallization rates and evidence for a rapid rise in seawater Mg over the last 10 million years. *Geochimica et Cosmochimica Acta 70*, 3883–3904.

Farrell, J.W., & Janecek, T.R. (1991). Late Neogene paleoceanography and paleoclimatology of the Northeast Indian Ocean (Site 758) In Weissel, J., Peirce, J., Taylor, E., Alt, J., et al. (Eds.), Proceedings of the Ocean Drilling Program, Scientific Results (pp. 297–355) College Station, TX: Ocean Drilling Program.

Fedorov, A.V., Brierley, C.M., Lawrence, K.T., Liu, Z., Dekens, P.S., & Ravelo, A.C. (2013). Patterns and mechanisms of early Pliocene warmth. *Nature 496*, 43–49.

Fedorov, A.V., Dekens, P.S., McCarthy, M., Ravelo, A.C., deMenocal, P.B., Barreiro, M., et al. (2006). The Pliocene Paradox (Mechanisms for a Permanent El Nino). *Science 312*, 1485–1489.

Fehrenbacher, J., Martin, P. (2011). Western equatorial Pacific deep water carbonate chemistry during the Last Glacial Maximum and deglaciation: Using planktic foraminiferal Mg/Ca to reconstruct sea surface temperature and seafloor dissolution. *Paleoceanography 26*, 1–16. https://doi.org/10.1029/2010PA002035

Feng, R., Otto-Bliesner, B.L., Fletcher, T.L., Tabor, C.R., Ballantyne, A.P., & Brady, E.C. (2017). Amplified Late Pliocene terrestrial warmth in northern high latitudes from greater radiative forcing and closed Arctic Ocean gateways. *Earth and Planetary Science Letters 466*, 129–138. https://doi.org/10.1016/j.epsl.2017.03.006

Ford, H.L., & Ravelo, A.C. (2018). Estimates of Pliocene Tropical Pacific Temperature Sensitivity to Radiative Greenhouse Gas Forcing. *Paleoceanography and Paleoclimatology 18*, 1050. https://doi.org/10.1126/science.1246172

Ford, H.L., Ravelo, A.C., & Hovan, S. (2012). A deep Eastern Equatorial Pacific thermocline during the early Pliocene warm period. *Earth and Planetary Science Letters 355-356*, 152–161.

Ford, H.L., Ravelo, A.C., Dekens, P.S., LaRiviere, J.P., & Wara, M.W. (2015). The evolution of the equatorial thermocline and the early Pliocene El Padre mean state. *Geophysical Research Letters 42*, 4878–4887.

Gartner, S. (1989). Neogene Calcareous Nannofossil Biostratigraphy, Leg 116 (Central Indian Ocean) In *Proceedings of the Ocean Drilling Program, Scientific Results* (pp. 165–187). College Station, TX: Ocean Drilling Program.

Gelman, A., & Hill, J. (2006) *Data Analysis Using Regression and Multilevel/Hierarchical Models*. New York, NY: Cambridge University Press.

Gill, E.C., Rajagopalan, B., Molnar, P.H., Kushnir, Y., & Marchitto, T.M. (2016a). Reconstruction of Indian Summer Monsoon Winds and Precipitation over the past 10,000 Years using Equatorial Pacific SST Proxy Records. *Paleoceanography 32*, 195-216. https://doi.org/10.1002/2016PA002971

Gill, E.C., Rajagopalan, B., Molnar, P., & Marchitto, T.M. (2016b). Reduced-dimension reconstruction of the equatorial Pacific SST and zonal wind fields over the past 10,000 years using Mg/Ca and alkenone records. *Paleoceanography 31,* 928–952. https://doi.org/10.1002/2016PA002948

Goldner, A., Huber, M., Diffenbaugh, N., & Caballero, R. (2011). Implications of the permanent El Niño teleconnection “blueprint” for past global and North American hydroclimatology. *Climate of the Past 7,* 723–743. https://doi.org/10.5194/cp-7-723-2011

Goreau, T.J. (1977). Quantitative effects of sediment mixing on stratigraphy and biogeochemistry: a signal theory approach. *Nature 265,* 525–526.

Gourlan, A.T., Meynadier, L., & Allègre, C.J. (2008). Tectonically driven changes in the Indian Ocean circulation over the last 25 Ma: Neodymium isotope evidence. *Earth and Planetary Science Letters 267,* 353–364. https://doi.org/10.1016/j.epsl.2007.11.054

Groeneveld, J., Steph, S., Tiedemann, R., Garbe-Schonberg, D., Nurnberg, D., & Sturm, A. (2006). Pliocene mixed-layer oceanography for Site 1241, using combined Mg/Ca and δ^{18}O analyses of *Globigerinoides sacculifer*. In Tiedemann, R., Mix, A.C., Richter, C., & Ruddiman, W.F. (Eds.), *Proceedings of the Ocean Drilling Program* (Vol. 202, p. 1–27). College Station, TX: Ocean Drilling Program.

Gupta, A.K., & Thomas, E. (2003). Initiation of Northern Hemisphere glaciation and strengthening of the northeast Indian monsoon: Ocean Drilling Program Site 758, eastern equatorial Indian Ocean. *Geology 31,* 47–50.

Harada, N., Handa, N., Harada, K., & Matsuoka, H. (2001). Alkenones and particulate fluxes in sediment traps from the central equatorial Pacific. *Deep-Sea Research I 48,* 891–907.

Haywood, A.M., Dowsett, H.J., Otto-Bliesner, B., Chandler, M.A., Dolan, A.M., Hill, D.J., et al. (2010). Pliocene Model Intercomparison Project (PlioMIP): experimental design and boundary conditions (Experiment 1). *Geoscientific Model Development 3,* 227–242.

Haywood, A.M., Hill, D.J., Dolan, A.M., Otto-Bliesner, B.L., Bragg, F., Chan, W.L., et al. (2013). Large-scale features of Pliocene climate: results from the Pliocene Model Intercomparison Project. *Climate of the Past 9,* 191–209. https://doi.org/10.5194/cp-9-191-2013-supplement

Haywood, A.M., & Valdes, P.J. (2004). Modelling Pliocene warmth: contribution of atmosphere, oceans and cryosphere. *Earth and Planetary Science Letters 218,* 363–377.

Haywood, A.M., Valdes, P.J., & Peck, V.L. (2007). A permanent El Niño-like state during the Pliocene? *Paleoceanography 22,* 1-21. https://doi.org/10.1029/2006PA001323

Higgins, J., & Schrag, D.P. (2012). Records of Neogene seawater chemistry and diagenesis in deep-sea carbonate sediments and pore fluids. *Earth and Planetary Science Letters 357-358,* 386–396.

Horita, J., Zimmerman, H., & Holland, H.D. (2002). Chemical evolution of seawater during the Phanerozoic: Implications from the record of marine evaporites. *Geochimica et Cosmochimica Acta 66,* 3733–3756.

Hovan, S., & Rea, D.K. (1992). The Cenozoic Record of Continental Mineral Deposition on Broken and Ninetyeast Ridges, Indian Ocean: Southern African Aridity and Sediment Delivery from the Himalayas. *Paleoceanography 7,* 833–860. https://doi.org/10.1029/92PA02176

Howell, F.W., Haywood, A.M., Dowsett, H.J., & Pickering, S.J. (2016). Sensitivity of Pliocene Arctic climate to orbital forcing, atmospheric CO_2 and sea ice albedo parameterisation. *Earth and Planetary Science Letters 441*, 133–142. https://doi.org/10.1016/j.epsl.2016.02.036

Imbrie, J., & Kipp, N.G. (1971). A new micropaleontological method for quantitative paleoclimatology: Application to a late Pleistocene Caribbean core. In Turekian, K.K. (Ed.), *The Late Cenozoic Glacial Ages* (pp. 71–181). New Haven, CT: Yale University Press.

Julian, P.R., & Chervin, R.M. (1978). A study of the Southern Oscillation and Walker Circulation phenomenon. *American Meteorotological Society 106,* 1433–1451.

Kaplan, A., Cane, M.A., Kushni, Y., Clement, A.C., Blumenthal, M.B., & Rajagopalan, B. (1998). Analyses of global sea surface temperature 1856-1991. *Journal of Geophysical Research 103,* 18567–18589.

Karnauskas, K.B., Mittelstaedt, E., & Murtugudde, R. (2017). Paleoceanography of the eastern equatorial Pacific over the past 4 million years and the geologic origins of modern Galápagos upwelling. *Earth and Planetary Science Letters 460,* 22–28. https://doi.org/10.1016/j.epsl.2016.12.005

Kaufman, D.S., Schneider, D.P., McKay, N.P., Ammann, C.M., Bradley, R.S., Briffa, K.R., et al. (2009). Recent Warming Reverses Long-Term Arctic Cooling. *Science 325,* 1234–1236. https://doi.org/10.1051/0004-6361:20065200

Kim, J.-H., Schouten, S., Hopmans, E.C., Donner, B., Sinninghe Damsté, J.S. (2008). Global sediment core-top calibration of the TEX86 paleothermometer in the ocean *Geochimica et Cosmochimica Acta 72(4),* 1154–1173. https://doi.org/10.1016/j.gca.2007.12.010

Kim, J.-H., van der Meer, J., Schouten, S., Helmke, P., Willmott, V., Sangiorgi, F., et al. (2010). New indices and calibrations derived from the distribution of crenarchaeal isoprenoid tetraether lipids: Implicationsfor past sea surface temperature reconstructions. *Geochimica et Cosmochimica Acta 74,* 4639–4654. https://doi.org/10.1016/j.gca.2010.05.027

Krishna-Kumar, K., Rajagopalan, B., Hoerling, M., Bates, G., & Cane, M. (2006). Unraveling the Mystery of Indian Monsoon Failure During El Niño. *Science 314,* 113–115. https://doi.org/10.1126/science.1131914

Lawrence, K.T., Liu, Z., & Herbert, T.D. (2006). Evolution of the Eastern Tropical Pacific Through Plio-Pleistocene Glaciation. *Science 312,* 79–83.

Lea, D.W., Mashiotta, T.A., & Spero, H.J. (1999). Controls on magnesium and strontium uptake in planktonic foraminifera determined by live culturing. *Geochimica et Cosmochimica Acta 63,* 2369–2379. https://doi.org/10.1016/S0016-7037(99)00197-0

Leduc, G., Schneider, R., Kim, J.H., & Lohmann, G. (2010). Holocene and Eemian sea surface temperature trends as revealed by alkenone and Mg/Ca paleothermometry. *Quaternary Science Reviews 29(7-8),* 989–1004. https://doi.org/10.1016/j.quascirev.2010.01.004

Lee, T.C.K., Zwiers, F.W., & Tsao, M. (2008). Evaluation of proxy-based millennial reconstruction methods. *Climate Dynamics 31,* 263–281. https://doi.org/10.1007/s00382-007-0351-9

Lewis, E., and D. W. R. Wallace (1998), Program developed for CO2 system calculations, ORNL/CDIAC-105, Carbon Dioxide Information Analysis Center, Oak Ridge National Laboratory, U.S. Department of Energy, Oak Ridge, TN.

Li, B., Nychka, D.W., & Ammann, C.M. (2010). The Value of Multiproxy Reconstruction of Past Climate. *Journal of the American Statistical Association 105,* 883–895. https://doi.org/10.1198/jasa.2010.ap09379

Loader, C.R. (1996). Local likelihood density estimation. *The Annals of Statistics 24,* 1602–1618.

Lowenstein, T.K., Timofeeff, M., Brennan, S.T., Hardie, L.A., & Demicoo, R.V. (2001). Oscillations in Phanerozoic seawater chemistry: Evidence from fluid inclusions. *Science 294*, 1086–1088.

Lunt, D.J., Foster, G.L., Haywood, A.M., & Stone, E.J. (2008). Late Pliocene Greenland glaciation controlled by a decline in atmospheric CO_2 levels. *Nature 454,* 1102–1105.

Luterbacher, J., Dietrich, D., Xoplaki, E., Grosjean, M., & Wanner, H. (2004). European Seasonal and Annual Temperature Variability, Trends, and Extremes Since 1500. *Science 303*, 1499–1503.

Mann, M.E., Bradley, R.S., & Hughes, M.K. (1998). Global-scale temperature patterns and climate forcing over the past six centuries. *Nature 392,* 779–787.

Mann, M.E., Zhang, Z., Hughes, M.K., Bradley, R.S., Miller, S.K., Rutherford, S., et al. (2008). Proxy-based reconstructions of hemispheric and global surface temperature variations over the past two millennia. *Proceedings of the National Academy of Sciences 105,* 13252–13257.

Marlowe, I.T., Brassell, S.C., Eglinton, G., & Green, J.C. (1984). Long chain unsaturated ketones and esters in living algae and marine sediments. *Organic Geochemistry 6,* 135–141.

Martínez-Botí, M.A., Foster, G.L., Chalk, T.B., Rohling, E.J., Sexton, P.F., Lunt, D.J., et al. (2015). Plio-Pleistocene climate sensitivity evaluated using high-resolution CO_2 records. *Nature 518,* 49–54. https://doi.org/10.1038/nature14145

Medina-Elizalde, M., Lea, D.W., & Fantle, M.S. (2008). Implications of seawater Mg/Ca variability for Plio-Pleistocene tropical climate reconstruction. *Earth and Planetary Science Letters 269*, 585–595.

Mehrbach, C., Culberson, C.H., Hawley, J.E., & Pytkowicz, R.M. (1973). Measurement of the apparent dissociation constants of carbonic acid in seawater at atmospheric pressure. *Limnology and Oceanography 18,* 897–907.

Mekik, F., François, R., & Soon, M. (2007). A novel approach to dissolution correction of Mg/Ca-based paleothermometry in the tropical Pacific. *Paleoceanography 22.* 1-12. https://doi.org/10.1029/2007PA001504

Moberg, A., Sonechkin, D.M., Holmgren, K., Datsenko, N.M., & Karlén, W. (2005). Highly variable Northern Hemisphere temperatures reconstructed from low- and high-resolution proxy data. *Nature 433*, 613–617. https://doi.org/10.1126/science.290.5499.2133

Molnar, P., & Cane, M.A. (2002). El Niño's tropical climate and teleconnections as a blueprint for pre-Ice Age climates. *Paleoceanography 17,* 1–13.

Molnar, P., & Cane, M.A. (2007). Early Pliocene (pre–Ice Age) El Niño–like global climate: Which El Niño? *Geosphere 3,* 337-365. https://doi.org/10.1130/GES00103.1

Müller, P., & Fischer, G. (2001). A 4-year sediment trap record of alkenones from the filamentous upwelling region off Cape Blanc, NW Africa and a comparison with distributions in underlying sediments. *Deep Sea Research Part I: Oceanographic Research Papers 48,* 1877–1903. https://doi.org/10.1016/S0967-0637(00)00109-6

Müller, P., Kirst, G., Gotz, R., von Storch, I., & Rosell-Mele, A. (1998). Calibration of the alkenone paleotemperature index $U^{K'}_{37}$ based on core-tops from the eastern South Atlantic and the global ocean (60°N-60°S). *Geochimica et Cosmochimica Acta 62,* 1757–1772.

National Center for Atmospheric Research Staff (Eds). Last modified 31 Jan 2014. "The Climate Data Guide: GLODAP: GLobal Ocean Data Analysis Project for Carbon." Retrieved from https://climatedataguide.ucar.edu/climate-data/glodap-global-ocean-data-analysis-project-carbon.

Nürnberg, D., Bijma, J., & Hemleben, C. (1996). Assessing the reliability of magnesium in foraminiferal calcite as a proxy for water mass temperatures. *Geochimica et Cosmochimica Acta 60,* 803–814. https://doi.org/10.1016/0016-7037(95)00446-7

Ohkouchi, N., Kawamura, K., Kawahata, H., & Okada, H. (1999). Depth ranges of alkenone production in the central Pacific Ocean. *Global Biogeochemical Cycles 13,* 695–704.

O'Brien, C.L., Foster, G.L., Martínez-Botí, M.A., Abell, R., Rae, J.W.B., & Pancost, R.D. (2014). High sea surface temperatures in tropical warm pools during the Pliocene. *Nature Geoscience 7(8)*, 606–611. https://doi.org/10.1038/NGEO2194

Pagani, M., Liu, Z., Lariviere, J., & Ravelo, A.C. (2010). High Earth-system climate sensitivity determined from Pliocene carbon dioxide concentrations. *Nature Geoscience 3,* 27–30.

Pälike, H., et al. (2012). A Cenozoic record of the equatorial Pacific carbonate compensation depth. *Nature 488,* 609–614. https://doi.org/10.1038/nature11360

Philander, S.G., & Fedorov, A.V. (2003). Role of tropics in changing the response to Milankovich forcing some three million years ago. *Paleoceanography 18,* 1–11.

Prahl, F.G., & Wakeham, S.G. (1987). Calibration of unsaturation patterns in long-chain ketone compositions for paleotemperature assessment. *Nature*, *330(26)*, 367–369.

Prell, W.L., & Kutzbach, J.E. (1997). The Impact of Tibet-Himalayan Elevation on the Sensitivity of the Monsoon Climate System to Changes in Solar Radiation. In Ruddiman, W.F. (Ed.), *Tectonic Uplift and Climate Change* (pp. 171–201). New York, NY: Plenum Press.

R Core Team (2014), *R: A Language and Environment for Statistical Computing*, R Foundation for Stat. Comput., Vienna.

Rae, J.W.B., Sarnthein, M., Foster, G.L., Ridgwell, A., Grootes, P.M., & Elliott, T. (2014). Deep water formation in the North Pacific and deglacial CO_2 rise. *Paleoceanography 29,* 645–667. https://doi.org/10.1002/2013PA002570

Rausch, S., Bohm, F., Bach, W., Klugel, A., & Eisenhauer, A. (2012). Calcium carbonate veins in ocean crust record a threefold increase of seawater Mg/Ca in the past 30 Million years. *Earth and Planetary Science Letters 362*, 215–224. https://doi.org/10.1016/j.epsl.2012.12.005

Ravelo, A.C., Dekens, P.S., & McCarthy, M. (2006). Evidence for El Niño–like conditions during the Pliocene. *GSA Today 16*, 4–11.

Ravelo, A.C., Lawrence, K.T., Fedorov, A.V., & Ford, H.L. (2014). Comment on "A 12-million-year temperature history of the tropical Pacific Ocean." *Science 346,* 1–5. https://doi.org/10.1126/science.1257618

Rea, D.K. (1992). Delivery of Himalayan sediment to the northern Indian Ocean and its relation to global climate, sea level, uplift, and seawater Strontium. In Duncan, R.A., et al. (Eds.), *Synthesis of Results from Drilling in the Indian Ocean* (pp. 377–402). American Geophysical Union: Washington, DC.

Rongstad, B.L., Marchitto, T.M., & Herguera, J.C. (2017). Understanding the effects of dissolution on the Mg/Ca paleothermometer in planktic foraminifera: Evidence from a novel individual foraminifera method. *Paleoceanography 193*, 1–17. https://doi.org/10.1016/j.epsl.2007.03.025

Ropelewski, C.F., & Halpert, M.S. (1996). Quantifying Southern Oscillation-precipitation relationships. *Journal of Climate 9,* 1043–1059.

Rosenthal, Y., Lohmann, G.P., Lohmann, K.C., & Sherrell, R.M. (2000). Incorporation and preservation of Mg in *Globigerinoides sacculifer*: Implications for reconstructing the temperature and $^{18}O/^{16}O$ of seawater. *Paleoceanography 15,* 135–145.

Salzmann, U., Dolan, A.M., Haywood, A.M., Chan, W.-L., Voss, J., Hill, D.J., et al. (2013). Challenges in quantifying Pliocene terrestrial warming revealed by data–model discord. *Nature Climate Change 3,* 969–974. https://doi.org/10.1038/nclimate2008

Salzmann, U., Williams, M.R., Haywood, A.M., Johnson, A.L.A., Kender, S., & Zalasiewicz, J. (2011). Climate and environment of a Pliocene warm world. *Palaeogeography, Palaeoclimatology, Palaeoecology 309,* 1–8.

Sanyal, P., Bhattacharya, S.K., & Prasad, M. (2005). Chemical diagenesis of Siwalik sandstone: Isotopic and mineralogical proxies from Surai Khola section, Nepal. *Sedimentary Geology 180,* 57–74. https://doi.org/10.1016/j.sedgeo.2005.06.005

Schiebel, R., Bijma, J., & Hemleben, C. (1997). Population dynamics of the planktic foraminifer *Globigerina bulloides* from the eastern North Atlantic. *Deep-Sea Research II 44,* 1701–1713.

Schiffelbein, P. (1984). Effect of benthic mixing on the information content of deep-sea stratigraphic signals. *Nature 311,* 651–653.

Schmuker, B. (2000). Recent Planktic Foraminifera in the Caribbean Sea: Distribution, Ecology and Taphonomy (Doctoral Dissertation). Retrieved from ETH Zurich Research

Collection (https://doi.org/10.3929/ethz-a-003887547). Eidgenoessisschen Technischen Hochschule: Zurich.

Schmuker, B., & Schiebel, R. (2002). Planktic foraminifers and hydrography of the eastern and northern Caribbean Sea. *Marine Micropaleontology 46,* 387–403.

Schouten, S., Schouten, S., Hopmans, E.C., Schefuß, E., & Sinninghe Damsté, J.S. (2002). Distributional variations in marine crenarchaeotal membrane lipids: A new tool for reconstructing ancient sea water temperatures? *Earth and Planetary Science Letters 204,* 265–274.

Seki, O., Foster, G.L., Schmidt, D.N., Mackensen, A., Kawamura, K., & Pancost, R.D. (2010). Alkenone and boron-based pCO_2 records. *Earth and Planetary Science Letters 292,* 201–211.

Seki, O., Schmidt, D.N., Schouten, S., Hopmans, E.C., Sinninghe Damsté, J.S., & Pancost, R.D. (2012). Paleoceanographic changes in the Eastern Equatorial Pacific over the last 10 Myr. *Paleoceanography 27,* 1–14.

Shukla, S.P., Chandler, M.A., Jonas, J., Sohl, L.E., Mankoff, K., & Dowsett, H. (2009). Impact of a permanent El Niño (El Padre) and Indian Ocean Dipole in warm Pliocene climates. *Paleoceanography 24,* 1–12. https://doi.org/10.1098/rsta.2008.0224

Shukla, S.P., Chandler, M.A., Rind, D., Sohl, L.E., Jonas, J., & Lerner, J. (2011). Teleconnections in a warmer climate: the Pliocene perspective. *Climate Dynamics 37,* 1869–1887. https://doi.org/10.1038/nature08316

Smith, T.M., Reynolds, R.W., Peterson, T.C., & Lawrimore, J. (2008). Improvements to NOAA's Historical Merged Land–Ocean Surface Temperature Analysis (1880–2006). *Journal of Climate 21,* 2283–2296. https://doi.org/10.1175/2007JCLI2100.1

Steph, S., Tiedemann, R., Prange, M., Groeneveld, J., Nürnberg, D., Reuning, L., et al. (2006). Changes in Caribbean surface hydrography during the Pliocene shoaling of the Central American Seaway. *Paleoceanography 21(4),* 1-25.

Steph, S., Tiedemann, R., Prange, M., Groeneveld, J., Schulz, M., Timmermann, A., et al. (2010). Early Pliocene increase in thermohaline overturning: A precondition for the development of the modern equatorial Pacific cold tongue. *Paleoceanography 25,* 1-25.

Thompson, P.R., & Saito, T. (1974). Pacific Pleistocene sediments: Planktonic foraminifera dissolution cycles and geochronology. *Geology 2,* 333–335. https://doi.org/10.1130/0091-7613

Tierney, J.E., & Tingley, M.P. (2018). BAYSPLINE: A New Calibration for the Alkenone Paleothermometer. *Paleoceanography and Paleoclimatology 33,* 281–301. https://doi.org/10.1016/j.palaeo.2005.11.033

Tierney, J.E., Haywood, A.M., Feng, R., Bhattacharya, T., and Otto-Bliesner, B.L. (2019). Pliocene warmth consistent with greenhouse gas forcing. *Geophysical Research Letters 46,* 1–26. https://doi.org/10.1029/2019GL083802.

Tingley, M.P., & Huybers, P. (2010). A Bayesian Algorithm for Reconstructing Climate Anomalies in Space and Time. Part I: Development and Applications to Paleoclimate

Reconstruction Problems. *Journal of Climate 23,* 2759–2781. https://doi.org/10.1175/2009JCLI3015.1

Trenberth, K., & Stepaniak, D.P. (2001). Indices of El Niño evolution. *Journal of Climate 14,* 1697–1701.

Vizcaíno, M., Rupper, S., & Chiang, J.C.H. (2010). Permanent El Niño and the onset of Northern Hemisphere glaciations: Mechanism and comparison with other hypotheses. *Paleoceanography 25,* 1–20. https://doi.org/10.1126/science.1059412

Volkman, J.K., Eglinton, G., Corner, E.D.S., & Forsberg, T.E.V. (1980). Long-chain alkenes and alkenones in the marine coccolithophorid *Emiliania huxleyi*. *Phytochemistry 19,* 2619–2622. https://doi.org/10.1016/S0031-9422(00)83930-8

Von Storch, H., & Zwiers, F.W. (2001). *Statistical Analysis in Climate Research* (pp.2000). Cambridge University Press: Cambridge.

Wang, L. (1994), Sea surface temperature history of the low latitude western Pacific during the last 5.3 million years, *Palaeoceanography, Palaeoclimatology, Palaeoecology*, *108*, 379–436.

Wara, M., & Ravelo, A.C. (2006). Data Report: Mg/Ca, Sr/Ca, Mn/Ca, and Oxygen and Carbon Isotope Records of Pliocene–Pleistocene Foraminifers from ODP Leg 202 Site 1237. In Tiedemann, R., Mix, A.C., Richter, C., and Ruddiman, W.F. (Eds.), *Proceedings of the Ocean Drilling Program, Scientific Results* (1-19 pp). Ocean Drilling Program, College Station, TX.

Wara, M.W., Ravelo, A.C., & Delaney, M.G.L. (2005). Permanent El Niño-Like Conditions During the Pliocene Warm Period. *Science 309*, 758–761. https://doi.org/10.1126/science.1112596

Wycech, J.B. (2017). Novel techniques and approaches to enhance the fidelity of foraminiferal paleoclimate records (Doctoral dissertation). Retrieved from Proquest (10623383). Madison, WI: University of Wisconsin-Madison.

Wycech, J.B., Kelly, D.C., Kitajima, K., Kozdon, R., Orland, I.J., & Valley, J.W. (2018). Combined Effects of Gametogenic Calcification and Dissolution on δ^{18}O Measurements of the Planktic Foraminifer *Trilobatus sacculifer*. *Geochemistry Geophysics Geosystems 18,* 1–15. https://doi.org/10.1029/2018GC007908

Zeebe, R.E., & Tyrrell, T. (2019). History of carbonate ion concentration over the last 100 million years II: Revised calculations and new data. *Geochimica et Cosmochimica Acta 257*, 373–392, https://doi.org/10.1016/j.gca.2019.02.041

Zhang, Y.G., Pagani, M., & Liu, Z. (2014). A 12-Million-Year Temperature History of the Tropical Pacific Ocean. *Science 344*, 84–87.

Zhang, X., Prange, M., Steph, S., Butzin, M., Krebs, U., Lunt, D.J., et al. (2012). Changes in equatorial Pacific thermocline depth in response to Panamanian seaway closure: Insights from a multi-model study. *Earth and Planetary Science Letters 317-318*, 76–84.

Zimmerman, H. (2000). Tertiary seawater chemistry: Implications from primary fluid inclusions in marine halite. *American Journal of Science 300,* 723–767.

Table 1. Equatorial Pacific SST Proxy Records

Site	Core	Latitude (°N)	Longitude (°E)	Water Depth (m)	Youngest Age (Ma)	Oldest Age (Ma)	Average Sampling Resolution (ka)	Reference*
				$U^{k'}_{37}$ Records				
1	ODP 846	-3.096	-90.818	3296	0.005	5.090	2	*Lawrence et al. (2006)*
				Mg/Ca (T. sacculifer) Records				
2	ODP 806	0.319	159.362	2520	0.019	5.138	12	*Wara et al. (2005)*
3	ODP 847	0.193	-95.320	3334	<0.01	5.393	21	*Wara et al. (2005)*
4	ODP 1237	-16.007	-76.378	3212	0.01	5.000	77	*Wara and Ravelo (2006)*
				TEX86 Records				
5	ODP 1241	5.843	-86.445	2027	0.094	9.535	201	*Seki et al. (2012)*
6	ODP 850	1.297	-110.521	3786	<0.01	11.88	150	*Zhang et al. (2014)*
7	ODP 1143	9.362	113.285	2772	0.06	4.98	43	*O'Brien et al. (2014)*
				Foraminiferal Assemblage Records				
8	DSDP 200	12.837	-156.783	1479	0.01	5.77	152	*Wang (1994)*
9	DSDP 289	-0.499	158.512	2206	<0.15	6.25	114	*Wang (1994)*

*Raw data provided in Table S1.

Figure 1. Equatorial Pacific maps of **a.** Niño Index regions (see Section 3.1 for coordinates), **b.** mean SSTs of the contemporary full field (1854-2018), and **c.** the limited field sites with Pliocene SST records. **d.** Raw SST time series. **e.** Smoothed SST records using a second order local polynomial with a local neighborhood of 20% nearest data points.

Figure 2. Model-data comparison of historical Niño Indices and El Niño events **a.** Historical time series of observed (black lines) and reconstructed (colored lines) Niño 4, Niño 3.4, Niño 3, and Niño 1+2 temperature anomalies. Vertical grey lines mark years of the two strongest El Niño events (dashed lines; 1983-1984, 1997-1998) and the two strongest La Niña years (solid lines; 1973-1974, 1988-1989, 2010-2011). **b.** Maps of actual and reconstructed SST anomalies for the 1982–1983 (left) and 1997–1998 (right) El Niño events.

Figure 3. Scatterplots of each SST proxy record from the equatorial Pacific (yellow) with the reconstructed SST values for the grid point nearest each record (blue). Error of the proxy-temperature calibration is shaded in light yellow around each record: ±1.5°C for $U^{k'}_{37}$ (Müller et al., 1998), ±1.2°C for Mg/Ca (Anand et al., 2003; Dekens et al., 2002), ±1.7 °C for TEX_{86} (Kim et al., 2010), and ±2.2°C for foraminiferal assemblages (Wang, 1994). Standard errors from the reconstructed model are shown as blue whiskers. Site numbers in the upper left correspond to those noted in Table 1 and Figure 1. EP=East Pacific, CP=Central Pacific, WP=West Pacific. The root mean square error (RMSE) quantifies how closely the reconstructed SSTs match the proxy SSTs (°C). The first two eigenvector values are noted at each location (EOF1 and EOF2) since the first two modes of the limited field were used for the PCA-based reconstruction.

Figure 4. a-e. Multiproxy reconstructed SST anomalies for 2, 3, 4, 4.3, and 5 Ma. Anomalies were defined relative to the 0-0.5 Ma average SST for each smoothed record. Circles note the proxy-based SST at each site using the same color bar. **f-j.** Standard errors calculated from 500 ensembles of each PC. Ensembles for the first three PCs generated from the linear regression. Ensembles for each of the remaining PCs generated by bootstrapping values from the original PCs at each grid point.

Figure 5. a. Plio-Pleistocene time series of Niño indices (temperature anomalies, left axis), the WTNI [(Niño 1+2) – WPAC] SST anomaly difference, and the absolute zonal SST difference ($\Delta SST_{West\text{-}East}$; right axis) calculated relative to the 0-0.5 Ma average value (8.4°C; see Section 4.2). The time series were calculated from PCA reconstructions at 0.02 Ma intervals. Shading around each time series is one standard error propagated from PCA reconstruction. **b.** Maps of the average SSTs from 0-0.5 Ma and the reconstructed SSTs at the $\Delta SST_{West\text{-}East}$ minima (4.1 Ma). Colors in circles show the proxy-based SST at each site and use the same color scale as in the maps.

Figure 6. Reconstruction of Indian Summer Monsoon strength and summary of previously published paleo-monsoon observations. **a.** Time series of reconstructed rainfall anomalies (percent on left axis, scaled on right axis; see Section 5.3 for reconstruction details). One standard error propagated from SST reconstruction is shown as the brown shaded area around the anomaly record. **b.** Summary of locations with sedimentary, geochemical, or foraminiferal proxy records that reflect hydrologic conditions, all of which indicate a weaker monsoon during the early Pliocene (Chang et al., 2010; Clift, 2006; Clift et al., 2008; Farrell & Janecek, 1991; Gartner, 1989; Gupta & Thomas, 2003; Hovan & Rea, 1992; Rea, 1992; Sanyal et al., 2005).

Figure A1. Comparison of Plio-Pleistocene SST records reconstructed using different calibrations on **a.** one $U^{k'}_{37}$ record from east Pacific ODP Site 846, and Mg/Ca records from **b.** west Pacific ODP Site 806 and **c-d.** east Pacific ODP sites 847 and 1237, respectively. Dashed grey horizontal line marks modern SST at each site. **a.** SSTs reconstructed using Müller et al. (1998) (black line) and BAYSPLINE calculated with prior standard deviations of 10°C (dark blue line) and 5°C (light blue line). Grey shading notes ±1.5°C error on the black line (Müller et al., 1998). **b-d.** SSTs calculated using the Dekens et al. (2002) calibration and corrections for dissolution based on water depth (grey lines) or the modern bottom-water ΔCO_3^{2-} value (red lines). Black line is the SST record used for this study using the depth-based dissolution correction and a paleo-Mg/Ca_{sw} record (Zeebe and Tyrell, 2019). Red error bars note Mg/Ca calibration error (±1.2°C SE; Anand et al., 2003; Dekens et al., 2002).

Figure A2. Eigenvalue spectra for the full SST field (black) and limited SST field (red). Asterisks note the variance explained by the first mode of each field. Plus signs mark the "knees," the points just before the noise floor (5%).

Figure A3. a-f. EOFs (shaded map) and normalized PCs (black time series) of the two leading modes of the PCA performed on the full field of contemporary equatorial Pacific SSTs. Limited SST field EOFs (circles, areas scaled to eigenvalues) and normalized PCs (red time series). All EOFs are multiplied by their respective eigenvalue (proportion of variance explained by that mode) to show relative strengths through subsequent modes. The first three eigenvalues are λ_1= 0.594, λ_2= 0.141, and λ_3= 0.074 for the full field PCA and $\lambda_1^{\dagger}$=0.737 and $\lambda_2^{\dagger}$=0.093 for the limited field PCA.

Figure A4. a-b. Model calibration statistics for the PCA-based SST model (shading and black contours) showing the skill of the models in reconstructing the contemporary data set. The *β* statistic represents the resolved variance captured by the reconstructed contemporary data. The R^2 equals the square of the correlation between the observed and reconstructed contemporary data. c-d. Model validation was performed by training the model on 1980–2013 data and using that model to validate SSTs from the period prior (1854–1979). The β and R^2 statistics again quantify model skill.

Figure 1.

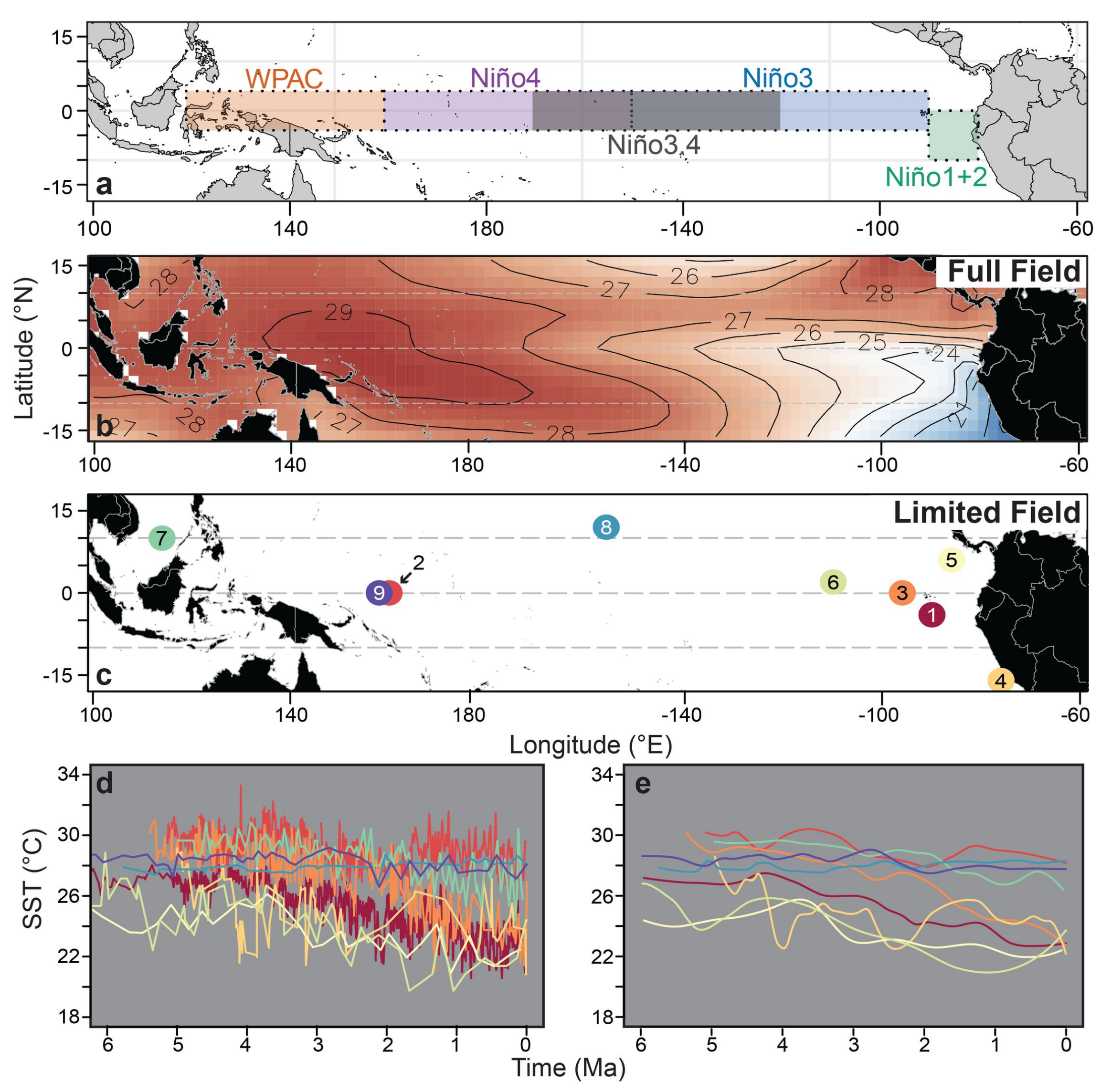

WPAC
Niño4
Niño3
Niño3.4
Niño1+2
a
b
Full Field
c
Limited Field
d
e
Latitude (°N)
Longitude (°E)
SST (°C)
Time (Ma)

Figure 2.

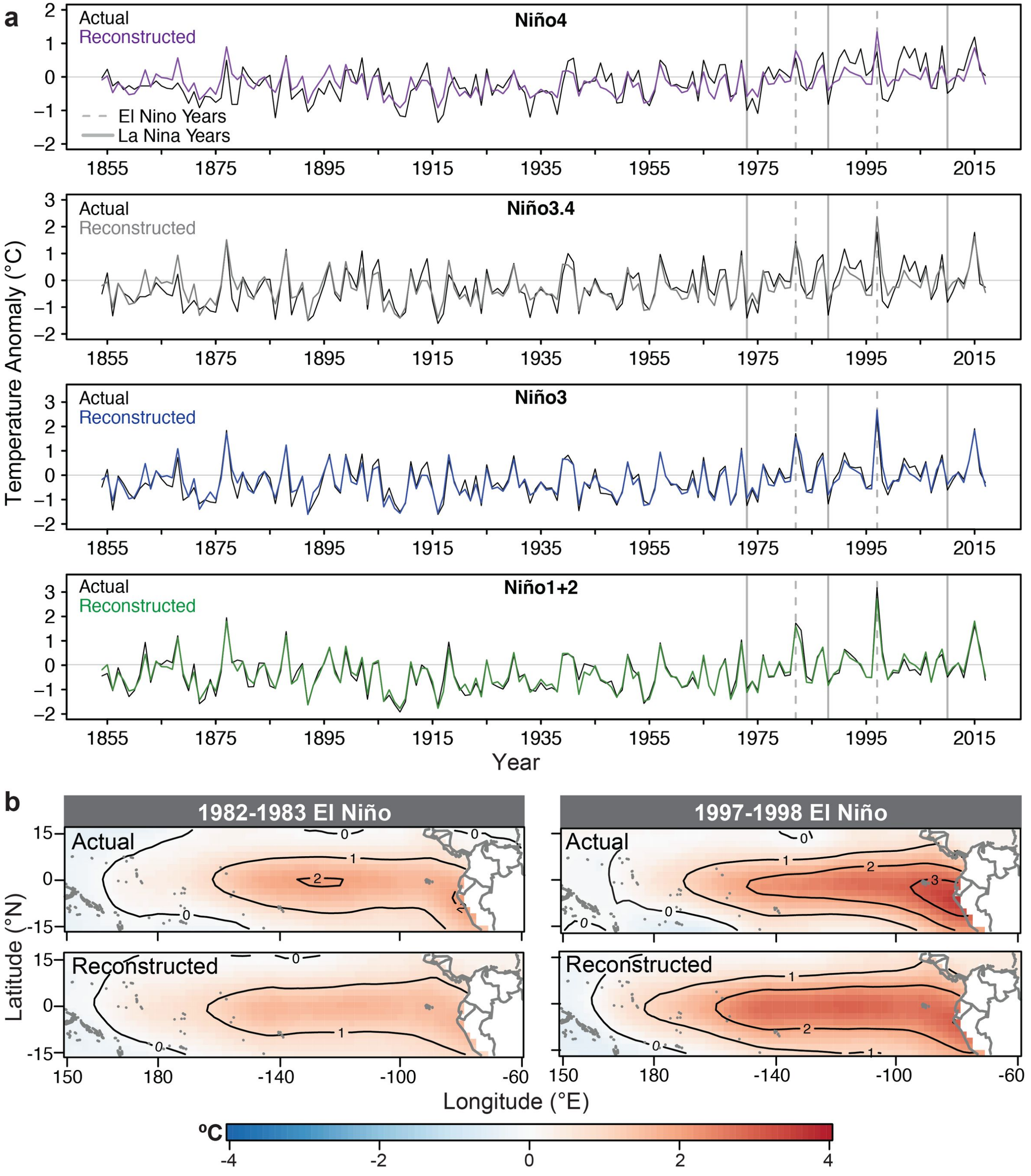
a
Niño4
Niño3.4
Niño3
Niño1+2
Actual
Reconstructed
El Nino Years
La Nina Years
Temperature Anomaly (°C)
Year
b
1982-1983 El Niño
1997-1998 El Niño
Latitude (°N)
Longitude (°E)
ºC

Figure 3.

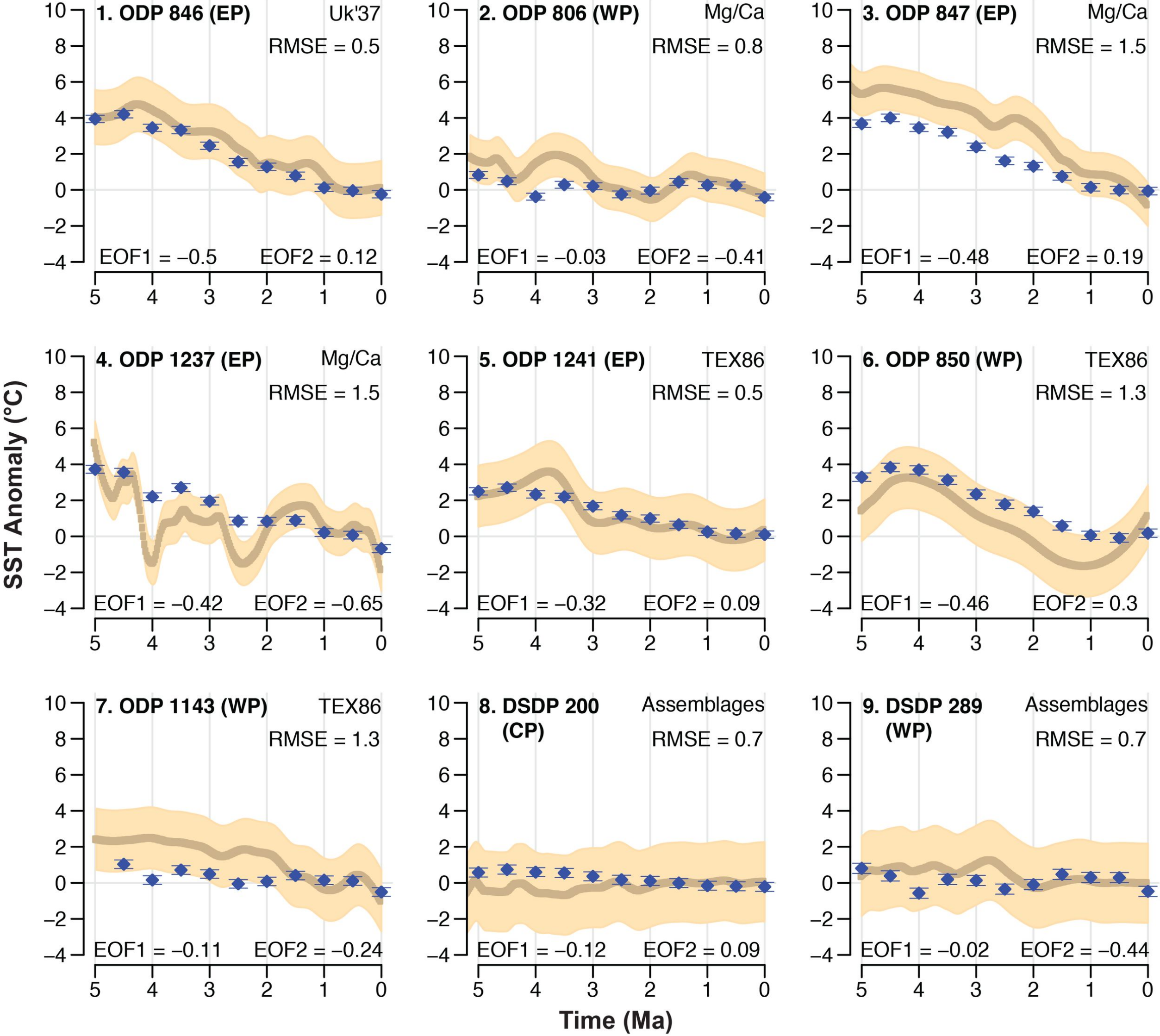
1. ODP 846 (EP)
Uk'37
RMSE = 0.5
EOF1 = –0.5
EOF2 = 0.12
2. ODP 806 (WP)
Mg/Ca
RMSE = 0.8
EOF1 = –0.03
EOF2 = –0.41
3. ODP 847 (EP)
Mg/Ca
RMSE = 1.5
EOF1 = –0.48
EOF2 = 0.19
4. ODP 1237 (EP)
Mg/Ca
RMSE = 1.5
EOF1 = –0.42
EOF2 = –0.65
5. ODP 1241 (EP)
TEX86
RMSE = 0.5
EOF1 = –0.32
EOF2 = 0.09
6. ODP 850 (WP)
TEX86
RMSE = 1.3
EOF1 = –0.46
EOF2 = 0.3
7. ODP 1143 (WP)
TEX86
RMSE = 1.3
EOF1 = –0.11
EOF2 = –0.24
8. DSDP 200 (CP)
Assemblages
RMSE = 0.7
EOF1 = –0.12
EOF2 = 0.09
9. DSDP 289 (WP)
Assemblages
RMSE = 0.7
EOF1 = –0.02
EOF2 = –0.44
SST Anomaly (°C)
Time (Ma)

Figure 4.

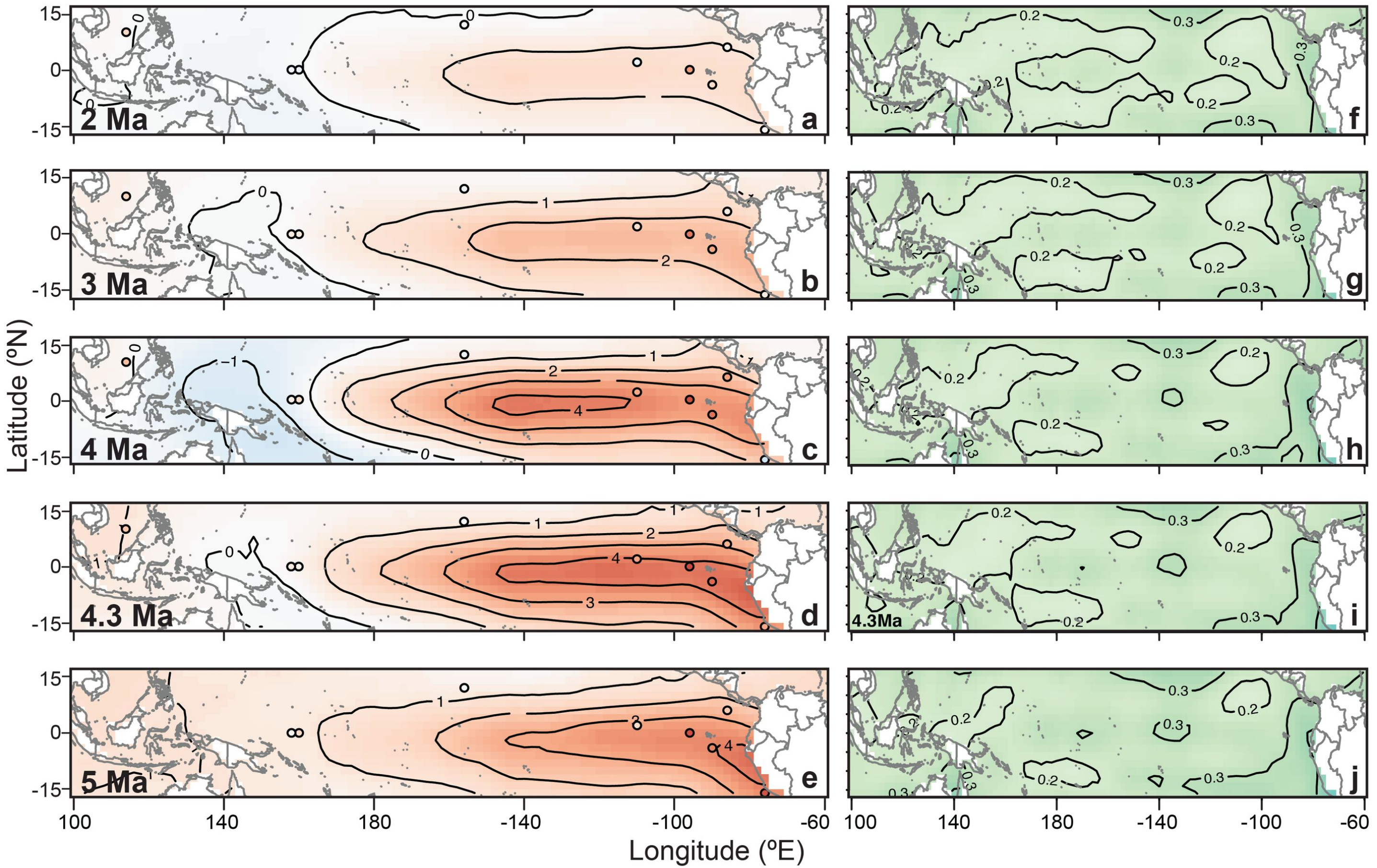

2 Ma
3 Ma
4 Ma
4.3 Ma
5 Ma
a
b
c
d
e
f
g
h
i
j
4.3Ma
Latitude (ºN)
Longitude (ºE)
15
0
-15
100
140
180
-140
-100
-60
0.2
0.3

Figure 5.

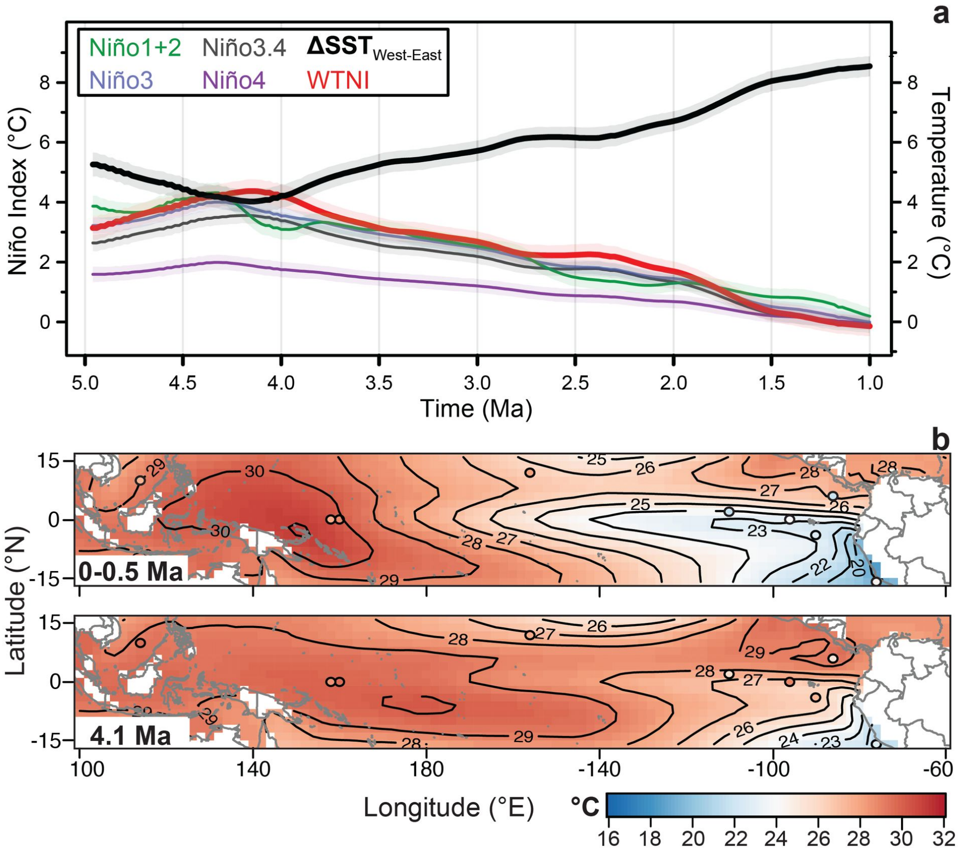

a
Niño1+2
Niño3.4
ΔSST West-East
Niño3
Niño4
WTNI
Niño Index (°C)
Temperature (°C)
Time (Ma)
b
0-0.5 Ma
4.1 Ma
Latitude (°N)
Longitude (°E)
°C

Figure 6.

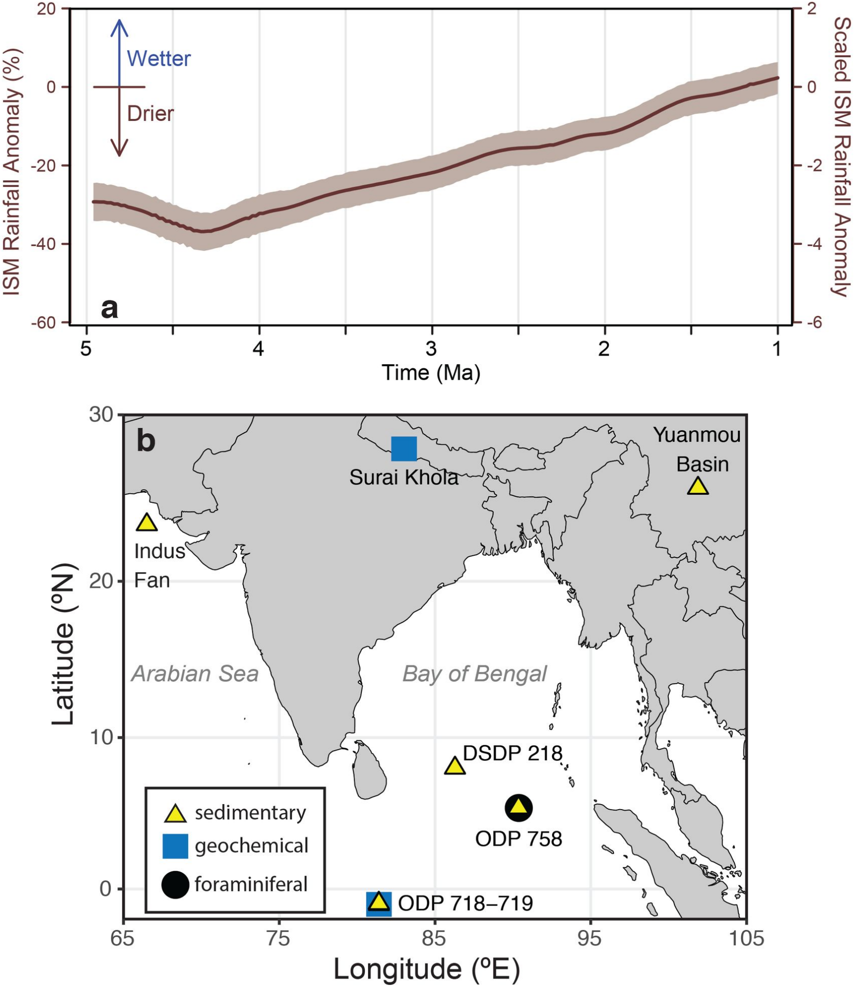
ISM Rainfall Anomaly (%)
Scaled ISM Rainfall Anomaly
Wetter
Drier
a
Time (Ma)
b
Surai Khola
Yuanmou Basin
Indus Fan
Arabian Sea
Bay of Bengal
DSDP 218
ODP 758
ODP 718–719
sedimentary
geochemical
foraminiferal
Latitude (ºN)
Longitude (ºE)

Figure A1.

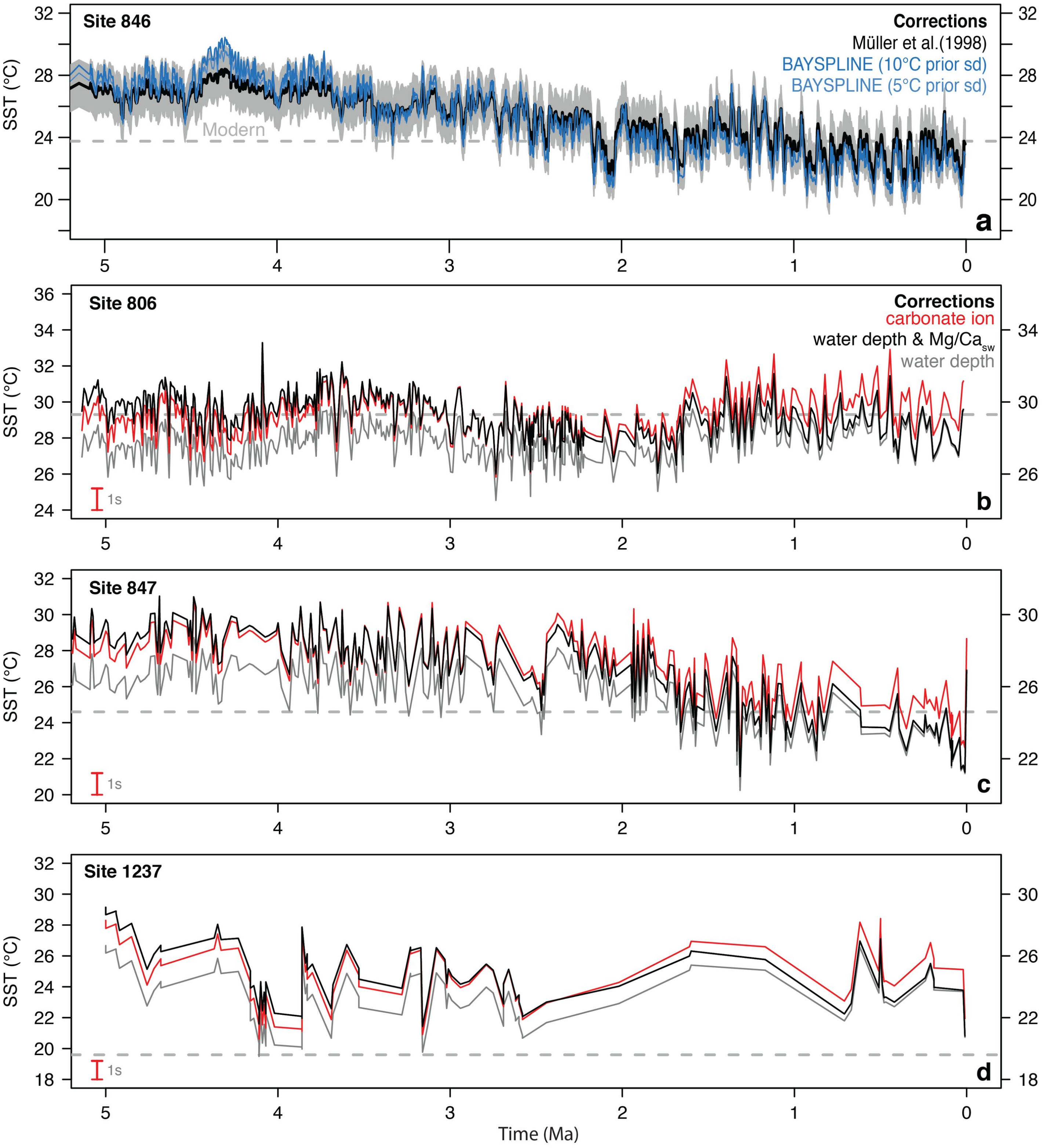
Site 846
Corrections
Müller et al.(1998)
BAYSPLINE (10°C prior sd)
BAYSPLINE (5°C prior sd)
Modern
SST (°C)
a
Site 806
Corrections
carbonate ion
water depth & Mg/Ca$_{sw}$
water depth
1s
b
Site 847
1s
c
Site 1237
1s
d
Time (Ma)

Figure A2.

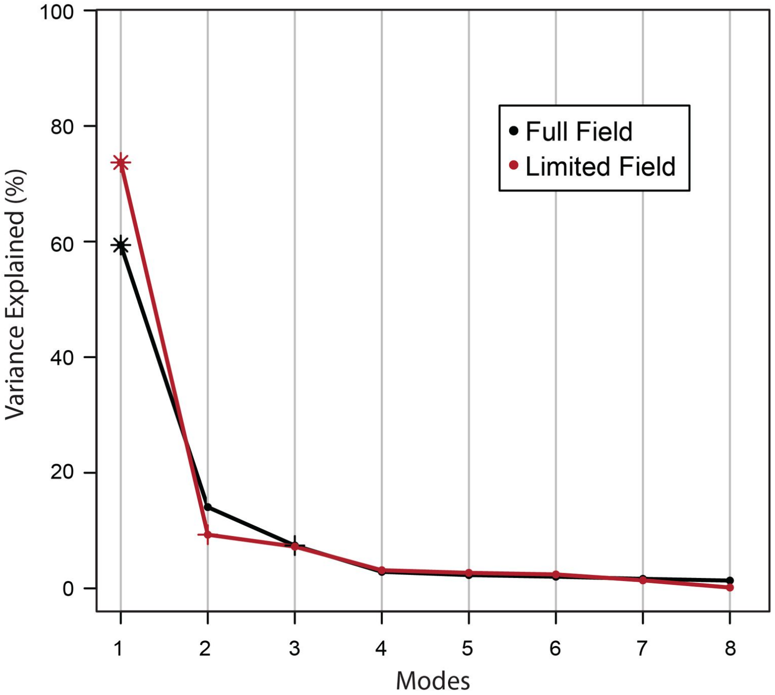

100
80
60
40
20
0
Variance Explained (%)
1
2
3
4
5
6
7
8
Modes
Full Field
Limited Field

Figure A3.

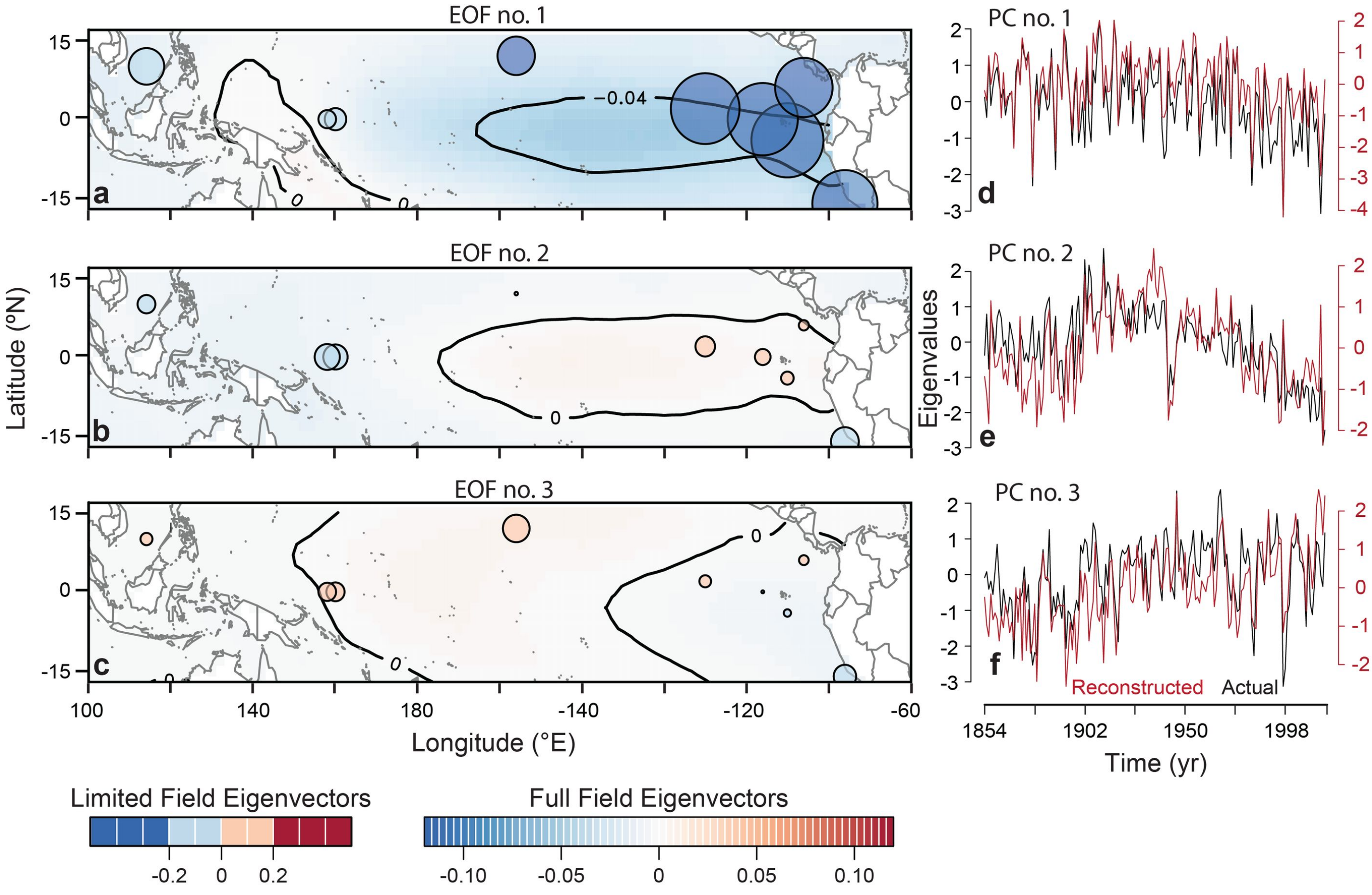
EOF no. 1
EOF no. 2
EOF no. 3
−0.04
0
a
b
c
Latitude (ºN)
Longitude (°E)
100
140
180
-140
-120
-60
15
0
-15
PC no. 1
PC no. 2
PC no. 3
d
e
f
Eigenvalues
Reconstructed
Actual
1854
1902
1950
1998
Time (yr)
Limited Field Eigenvectors
-0.2
0
0.2
Full Field Eigenvectors
-0.10
-0.05
0
0.05
0.10

Figure A4.

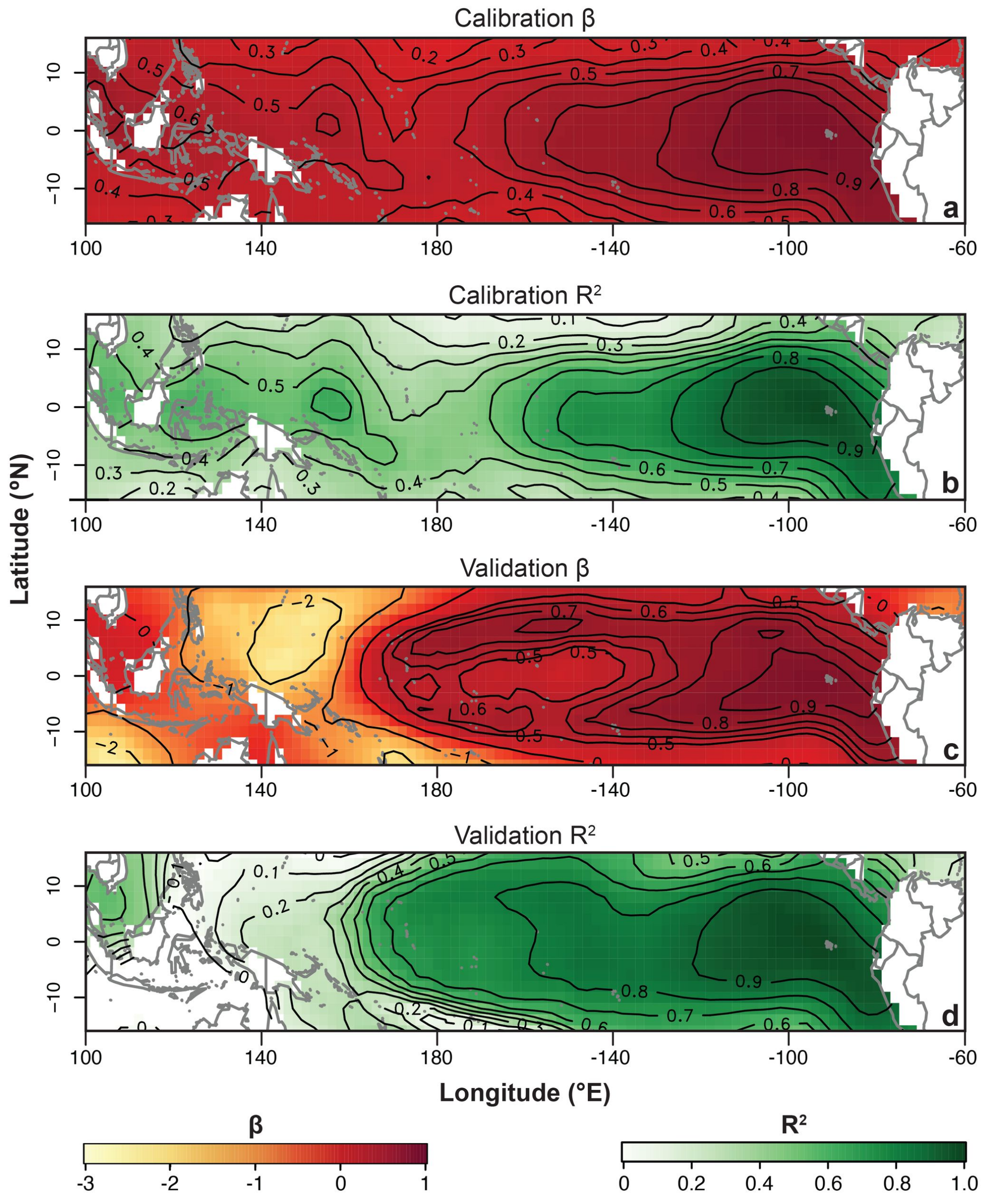

Calibration β
Calibration R²
Validation β
Validation R²
a
b
c
d
Latitude (°N)
Longitude (°E)
100
140
180
-140
-100
-60
10
0
−10
β
-3
-2
-1
0
1
R²
0
0.2
0.4
0.6
0.8
1.0